

AD-A179 663

FACILITIES AND INSTRUMENTATION ACQUIRED UNDER THE DOD  
INSTRUMENTATION GRA. (U) MASSACHUSETTS INST OF TECH  
CAMBRIDGE SPACE SYSTEMS LAB E F CRAWLEY ET AL.

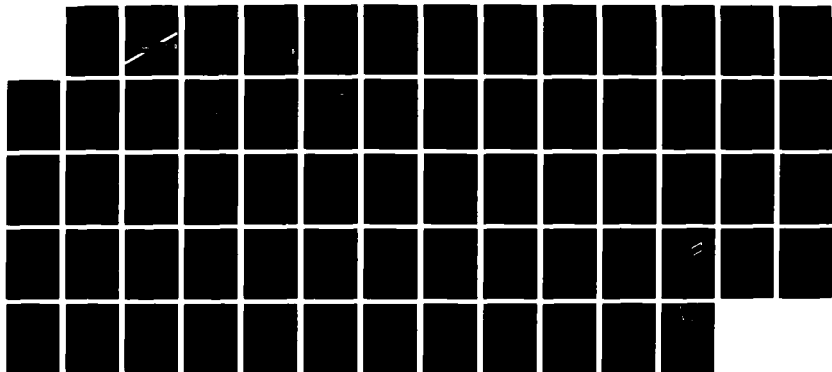
1/1

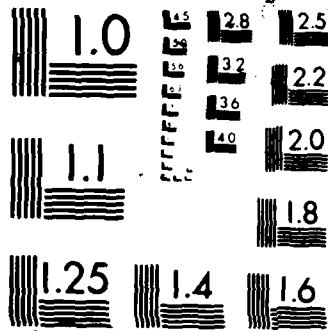
UNCLASSIFIED

22 JAN 87 MIT-SSL-3-87 AFOSR-TR-87-0425

F/G 20/11

NL





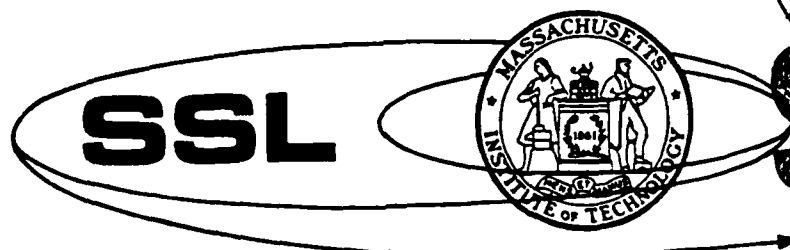
XEROCOPY RESOLUTION TEST CHART

AD-A179 663

DTIC FILE COPY  
AFOSR-TN- 87-0425

1. AUTHORITY		3. DISTRIBUTION/AVAILABILITY	
2. DOWNGRADING SCHEDULE		Approved for public release Unclassified/Unlimited distribution unlimited	
4. REPORT NUMBER(S)		5. MONITORING ORGANIZATION	
		AFOSR-TN-	
6a. ORGANIZATION	6b. OFFICE SYMBOL (If applicable)	7a. NAME OF MONITORING ORGANIZATION	
ASTRO MIT		AFOSR	
7b. ADDRESS (City, State and ZIP Code)			
2139		Bolling AFB Washington, DC 2033	

Approved for public  
distribution



SSL

DTIC  
ELECTE  
APR 24 1987

E

AIR FORCE OFFICE OF SCIENTIFIC RESEARCH (AFSC)  
NOTICE OF TRANSMITTAL TO DTIC  
This technical report has been reviewed and is  
approved for public release IAW AFR 190-12.  
Distribution is unlimited.  
MATTHEW J. KERPER  
Chief, Technical Information Division

SPACE SYSTEMS LABORATORY  
DEPT. OF AERONAUTICS AND ASTRONAUTICS  
MASSACHUSETTS INSTITUTE OF TECHNOLOGY  
CAMBRIDGE, MA 02139

87 4 23 149

Unclassified

SECURITY CLASSIFICATION OF THIS PAGE

## REPORT DOCUMENTATION PAGE

1a. REPORT SECURITY CLASSIFICATION Unclassified		1b. RESTRICTIVE MARKINGS	
2a. SECURITY CLASSIFICATION AUTHORITY		3. DISTRIBUTION/AVAILABILITY OF REPORT Approved for public release, Unclassified/Unlimited, distribution unlimited	
2b. DECLASSIFICATION/DOWNGRADING SCHEDULE		5. MONITORING ORGANIZATION REPORT NUMBER(S) <b>AFOSR-TN- 87-0425</b>	
4. PERFORMING ORGANIZATION REPORT NUMBER(S) MIT-SSL #3-87		7a. NAME OF MONITORING ORGANIZATION AFOSR	
3a. NAME OF PERFORMING ORGANIZATION Space Systems Lab Dept. of AERO and ASTRO MIT	3b. OFFICE SYMBOL (If applicable)	7b. ADDRESS (City, State and ZIP Code) Bolling AFB Washington, DC 20332-6448	
6c. ADDRESS (City, State and ZIP Code) 37-341 MIT Cambridge, MA 02139		7d. ADDRESS (City, State and ZIP Code) Bolling AFB Washington, DC 20332-6448	
8a. NAME OF FUNDING/SPONSORING ORGANIZATION AFOSR	8b. OFFICE SYMBOL (If applicable) NA	9. PROCUREMENT INSTRUMENT IDENTIFICATION NUMBER GRANT AFOSR-84-0197 83-0352	
8c. ADDRESS (City, State and ZIP Code) Bolling AFB Washington, DC 20332-6448		10. SOURCE OF FUNDING NOS.	
		PROGRAM ELEMENT NO. 6110ZF	PROJECT NO. 2917
		TASK NO. A-1	WORK UNIT NO.
11. TITLE (Include Security Classification) Department of Defense Instrumentation Grant, Final Report for Grant AFOSR-83-0352			
12. PERSONAL AUTHOR(S) Crawley, Edward F., Sawyer, George L., Miller, David W			
13a. TYPE OF REPORT Final	13b. TIME COVERED FROM 9/1/83 TO 5/31/85	14. DATE OF REPORT (Yr., Mo., Day) 87/1/22	15. PAGE COUNT 62
16. SUPPLEMENTARY NOTATION			
17. COSATI CODES		18. SUBJECT TERMS (Continue on reverse if necessary and identify by block number)	
FIELD	GROUP	SUB GR	
		Instrumentation Grant, Space Structures, equipment	
		Control of Flexible Structures, Instruments	
19. ABSTRACT (Continue on reverse if necessary and identify by block number) This report summarized the facilities and instrumentation acquired under the DOD Instrumentation Grant No. AFOSR-84-0197, monitored by AFOSR. It includes a short description of the apparatus, as well as a summary of the research projects on which it has been and will be used. This is followed by a detailed listing of the equipment actually purchased, its manufacturer and cost. <i>Key...</i>			
20. DISTRIBUTION/AVAILABILITY OF ABSTRACT UNCLASSIFIED/UNLIMITED <input type="checkbox"/> SAME AS RPT <input type="checkbox"/> DTIC USERS <input type="checkbox"/>		21. ABSTRACT SECURITY CLASSIFICATION Unclassified	
22a. NAME OF RESPONSIBLE INDIVIDUAL Dr. Anthony Amos	22b. TELEPHONE NUMBER (Include Area Code) 202-767-4937	22c. OFFICE SYMBOL AFOSR/NA	

1

Department of Defense  
Instrumentation Grant  
Final Report  
for Grant AFOSR 83-0352

Edward F. Crawley  
George L. Sarver III  
David W. Miller

SSL Report No. 3-87 January 1987  
Sponsored by AFOSR

Accession For	
NTIS GRA&I	<input checked="checked" type="checkbox"/>
DTIC TAB	<input type="checkbox"/>
Unannounced	<input type="checkbox"/>
Justification	
By	
Distribution/	
Availability Codes	
Dist	Avail and/or Special
A-1	

QUICK  
INSPECTED  
2

DTIC  
ELECTE  
S APR 24 1987 D  
E

## Contents

## Page

Summary	4
1. Description of facility and equipment	5
2. Related research	9
3. Equipment purchased	12

### Appendix 1:

"Theoretical and Experimental  
Investigation of Space Realiz-  
able Actuation for Passive and  
Active Structural Control."

### Appendix 2:

"A Procedure for Calculating the  
Damping in Multi-Element Space  
Structures."

## Summary

This report summarizes the facilities and instrumentation acquired under the DoD Instrumentation Grant No. AFOSR-<sup>83-0352</sup>84-0197, monitored by AFOSR. It includes a short description of the apparatus, as well as a summary of the research projects on which it has been and will be used. This is followed by a detailed listing of the equipment actually purchased, its manufacturer and cost.

## 1. Description of Facility and Equipment

The objective of the DoD Instrumentation Grant was to increase the capability of the Space Systems Laboratory to perform research in the area of the dynamics and control of flexible space structures.

As outlined in the original proposal of November 22, 1982, there were at that time a number of "component" level investigations being carried out at MIT. These were intended to resolve issues of structural modeling; control system design; and joint, sensor, and actuator design. It was desirable to integrate these various component level technologies into a larger scale experiment, in order to investigate schemes for active and passive control of space structures.

The specific objective of the Instrumentation Grant was to construct a nationally unique facility, which came to be known as the ASTROVAC, in which the hard vacuum and zero gravity of space could be simulated. In such a facility measurements on the dynamics of space structures in simulated space conditions could be made. A second objective was to build up the necessary equipment to conduct active control experiments on model structures in the laboratory at MIT. The facility and equipment to perform these experiments will be described below.



## ASTROVAC

The principal facility constructed under the Instrumentation Grant is the ASTROVAC, the Apparatus for Structural Testing and Research on On-Orbit Vibration And Control. The ASTROVAC is a ten foot diameter, 14 foot high vacuum test facility (Fig. 1) (budget item 1a).<sup>\*</sup> The facility can be pumped down to a vacuum level of  $10^{-1}$  torr in roughly one-half hour, using a mechanical vacuum pump (item 1b). This level of vacuum is sufficiently low to eliminate most air effects important in structural dynamic testing. When the cryogenic vacuum pump is used (item 1b), vacuums up to  $10^{-8}$  torr can be achieved, which nearly simulates the vacuum environment in low earth orbit. This level of vacuum is potentially important for studying out-gassing of structures and cold vacuum welding of joints.

The unique feature of the ASTROVAC is the lofting system (Fig. 2), (items 2a,b and c). This pneumatically driven system allows test specimens of up to 100 lbs weight to be lofted up inside the chamber. In this way the test specimen free falls through the vacuum for 1.4 seconds. During this time transient systems identification measurements can be made on the test article. Because it is in both vacuum and zero gravity, this is the closest earth based simulation of the orbital environment currently achievable.

---

<sup>\*</sup>Budget items refer to the Equipment Purchased Summary in Section 3.

In order to monitor and control the test, and take data on the response of the structure, a sophisticated control and data system was constructed (Fig. 3). This includes computer control of the experiment (item 4d), and a 16 channel high speed analog to digital data system (item 4c), and the associated signal amplifiers (item 4b) and filters (item 4a). A diagnostic oscilloscope is also included (item 4d). With this assembled equipment, the ASTROVAC can perform state-of-the-art experimentation on space structures.

#### Control Hardware

In order to develop a distributed processing approach to the control of flexible structures, a hierarchic microprocessor controller was developed (item 3c). This computer network is shown schematically in figure 4. Discrete time control was accomplished in one master and three slave 8088/8087 processors. Measurement information was exchanged between processors through dual access, shared memory space. Together with the four space realizable pivoted proof mass, actuators and inertial sensors (items 3a and b), this enabled research in the Space Systems Laboratory to be conducted in a number of new and unique control topics. A more complete description of the control hardware is contained in Appendix 1, which is a preprint of a paper by the authors, entitled "Theoretical and Experimental Investigation of Space Realizable Actuation for Passive and

Active Structural Control," to appear in the *AIAA Journal of Guidance, Control and Dynamics*.

## 2. Related Research

The research conducted with the ASTROVAC and the related control hardware spans a broad range of topics in the area of the dynamics and control of flexible structures. The principal use of the ASTROVAC has been in the experimental verification of ground- and space-based testing techniques aimed at measuring the damping in built-up multi-element space structures.

Under separate sponsorship an analytical procedure has been developed for estimating the damping in such multi-element space structures. Damping is an important parameter in the design of the high performance, closed loop control systems of precision spacecraft of interest to the DoD. In conjunction with this analysis, tests have been conducted in the ASTROVAC, in which the transient response of a truss member is recorded in order to obtain precise measurements of its material damping. A second experimental procedure known as the Force-State Mapping Technique has been used to identify the localized nonlinearities in joints of such space structures by mapping the force transmitted through the joint as a function of its mechanical state. The distributed material damping and appropriately linearized joint characteristics are then incorporated into a model of the space structure. This procedure is described in more detail in Appendix 2, which is a preprint of a paper by the authors

entitled, "A Procedure for Calculating the Damping in Multi-Element Space Structures," to appear in *Acta Astronautica*.

The role of the ASTROVAC is to provide an earth-based facility in which tests can be conducted to verify this calculation procedure, and to experiment with techniques for ground-based testing of space structures. To date a number of structures, prototypical of NASA Space Station hardware, have been tested. This work has primarily been sponsored by NASA Headquarters, under NASA Grant NAGW-21, with Mr. Sam Venneri serving as grant monitor, and by the McDonnell Douglas Astronautics Company, under IRAD funding, with Mr. James Peebles acting as contract monitor.

In addition, the ASTROVAC facility has been used to support preliminary ground based testing of three proposed shuttle flight experiments including: SAVE, the Space Station Structures and Assembly Verification Experiment, sponsored by the Space Station Projects Office of NASA Langley Research Center; COFS I, the first experiment in the Control of Flexible Structures experiment series, conducted by the COFS Program Office of NASA Langley Research Center; and MODE, the Mid-deck 0-Gravity Dynamics Experiment, proposed to NASA by MIT under the OAST In-Space Flight Experiments Program.

In addition, the ASTROVAC facility has been used to develop data in support of the design of COFS III, the scaled model Space Station structures experiment, conducted by the COFS Program Office at NASA Langley Research Center.

The related controls hardware has been used to support an AFOSR sponsored program in which inertial reaction devices were investigated for use as passive vibration absorbers and active control actuators for flexible space structures. Absorbers were designed for one- and two-degree of freedom structural representations. Proof of concept laboratory experiments were performed. The actuators developed and used were inertial reaction devices, which are space-realizable; i.e., capable of operating in the space environment. Damping of the structure was shown to significantly increase by using the devices passively, or actively, in conjunction with the distributed micro processor based controller. This work is detailed in Appendix 1.

The work was funded by AFOSR under Grant No.F49620-84-K-0010 entitled, "The Development of Intelligent Structural Elements for Use in Hierarchic Control of Flexible Space Structures." A continuation of this effort, which focuses on traveling wave concepts in structural dynamics and control is also sponsored by AFOSR under contract No.F49620-86-C-0039, both efforts were monitored by Dr. Anthony K. Amos.

In all, more than eight efforts involving four sponsors and five graduate students have made use of the experimental facilities created under the DoD Instrumentation Grant. There is every indication that this level of utilization will continue in the near future.

### 3.0 Equipment Purchased

Item	Vendor	Budgeted Amount	Actual Amount
1a. VACUUM VESSEL		50,000	
120" diameter, 168" high stainless steel vacuum chamber	Russell Engineering		47,111.00
Port blanks	Russell Engineering		2,126.75
Tank damping pads (Waffle Neoprene)	Fabreeka Products		183.09
Nuts & bolts	Russell Engineering		435.00
1b. VACUUM SYSTEM		41,500	
Kinney Model CC4030 close-coupled mechanical Vacuum booster pump.	Kinney Vacuum		12,797.46
CYRO-TORR 10 High Vacuum System	CTI-Cryogenics		12,500.00
Purge tube for Cryo-torr 10 pump	CTI-Cryogenics		326.37
Connectors	Columbia Connector Corp		151.98
Aluminum tubing	American Steel & Alum		224.62
Valves	Varian Associates		4,584.49
Filters	Filter Sales		707.00
Vacuum parts	Leybold Haraeus		245.17
ASA Flexible Connector	Stokes Div/Pennwalt Corp		831.94
Valves	Key Vacuum Products		1,098.44
Steel pipe	J.T. Ryerson & Co		128.94
Vacuum gages	Granville Phillips		1,238.97
Connector	Cambridge Valve & Fitting		22.08
2a. & 2b. LAUNCH MECHANISM		16,780	
Piston Assembly fabricated	High Vacuum Equip Corp		11,620.00
101 SRPA Shaker Unit	Ling Electronics		10,652.41
Motors for data link	AST/Servo Systems, Inc.		2,550.70
BNC Plugs	Trompeter Electronics		156.36
Vacuum feedthroughs	Varian		2,376.64
Potter Brumfield Solid State Relays	Relay Specialties Inc		59.25
Amphenol BNC Receptable	Gerber Electronics		53.90
Lemo connector series 00 and receptable	Zieco Inc		784.40
Time Delay Relays	Allied Electronics		149.85
Computation time			201.65
2a. LAUNCH MECHANISM CONTROLLER		995	
Wavetek Model 132 VCG/Noise Generator	Wavetek		2,050.44
2c. MANIPULATOR		4,350	0.00

3a. ACCELEROMETERS (SENSORS)		18,050	
Laser Vibrometer system	Disa Electronics		25,818.88
3b. ACTUATORS		10,000	
PA-601 Power amplifier	EG&G Torque Systems	-	482.46
1.75 lb 110 on-in peak stall torque motor	PMI Motors		276.46
QT-1401 Frameless Torque motor & TG-0702 Frameless Tachometer	Inland Motors		894.10
Pittman Servo Motors	Pittman Corp		158.84
Cable	Sager Co		166.23
TG-0702 Frameless Tachometers	Inland Motors		913.51
Connectors	Lemo		682.12
200-M608 Rotary Potentiometers	Maurey Instruments Corp		888.71
PL20-5 Crimp Wrench	Trompeter Electronics		198.74
110 Watt Power Op Amp & heat sinks	EG&G Torque Systems		1,030.63
Power Supplies	Lambda Electronics		984.66
Panel Mounts	Lemo		215.10
Sockets, Heat sinks and 100 watt power amps	EG&G Torque Systems		1,278.12
Power amplifier, dual polarity supply, & heat sink	EG&G Torque Systems		1,799.09
.01 OHM, 3.25 watt fractional resistors	Sterling Electronics		39.50
Angular Displacement Transducer	Trans-Tek Inc		251.29
Rotary Potentiometer	Maurey Instrument		224.68
3c. MICROPROCESSOR FOR STRUCTURE CONTROL		29,650	
ZT8830 Slave Processor	Ziatech Corp		452.25
ISBX-311 Analog Input Multi-module board	Hamilton/Avnet		612.57
Intel #ISBX 328 Analog Outputs & Intel #ISBX 321 Fixed/floating math	Hamilton/Avnet		2,555.67
Intel #ISBX-328 Analog output	Hamilton/Avnet		754.71
ZT8830 I/O slave control processor	Ziatech		457.25
Intel #ISBX-311 Analog input	Pioneer-Standard Electronics		641.44
ADSP-1009 JD 12x12 Bit CMOS Mult/Acc	Analog Devices		376.29
ER32-R Card Cage, 7101-8 Slot Motherboard, 12v power supply&terminator card	PRO-LOG		696.00
4a. BESSEL FILTERS		8,850	
Model #844 PBL-4 Module Bessel Filters	Frequency Devices		2,252.83
Amphenol BNC receptacles & connectors	Gerber Electronics		221.91
Dip switches and Bourns S/P isolated resistors	Gerber Electronics		81.32
Vectorboards	Gerber Electronics		48.51
Vector NIM modules	Newark Electronics		961.81
LNS-215 Power supplies	Lambda Electronics		207.58
Relay Racks and casters	Gerber Electronics		1,075.84



4b. AMPLIFIERS		4,000	
Model 2120 Strain Gage Conditioner/Amplifier with digital readout	Measurements Group		7,015.67
8AD521 JD IC's	Analog Devices		269.49
Receptacles, buttons, switches, dials, wire and connector amphenols	Gerber Electronic		1,180.62
Power supplies	Lambda Electronics		595.38
Vector modules	Vector Electronics		257.24
Receptacles and plugs	Lemo		206.94
Rotary switches	Gerber Electronics		91.73
Resistors and capacitors	Newark Electronics		29.18
15 volt power supplies	Lambda Electronics		234.40
Bourns pots	Gerber Electronics		271.26
4c. A/D CONVERTER		13,050	
Model 8601 Programmable Function Generator & dual port memory # 8201/12	LeCroy		3,802.71
Model 8212A Transient recorder	LeCroy		14,559.39
4d. COMPUTER		17,500	
IBM Personal Computer Model 087 XT	IBM Product Center		3,759.20
IBM Personal Computer Model 087 XT	Sears Business System Center		3,711.19
8087-3 Math Coprocessor Chips & Microsoft Fortran 3.2	Micro Ware		615.50
National Instruments GPIB-PC Interface card	Scheinfein Associates		590.67
4-device T-switch for 25 line RS232 cables	Inmac		340.91
Selanar SG-100 main graphics board & SG105 communications board	Data Access Systems		982.99
Epston LQ-1500 Printer	The Bottom Line		1,229.88
Zenith amber monitor	Lechemre		109.99
National Instruments GPIB-PC Interface card	Scheinfein Associates		533.63
Quadboards, no RAM	Conroy LaPointe		442.90
64K memory RAM upgrade	Microway		578.00
4e. DIAGNOSTIC OSCILLOSCOPE		10,195	
Digital Oscilloscope	Nicolet		11,529.65
TOTALS		224,920	216,006.52

AUTHORIZED AMOUNT - \$216,000

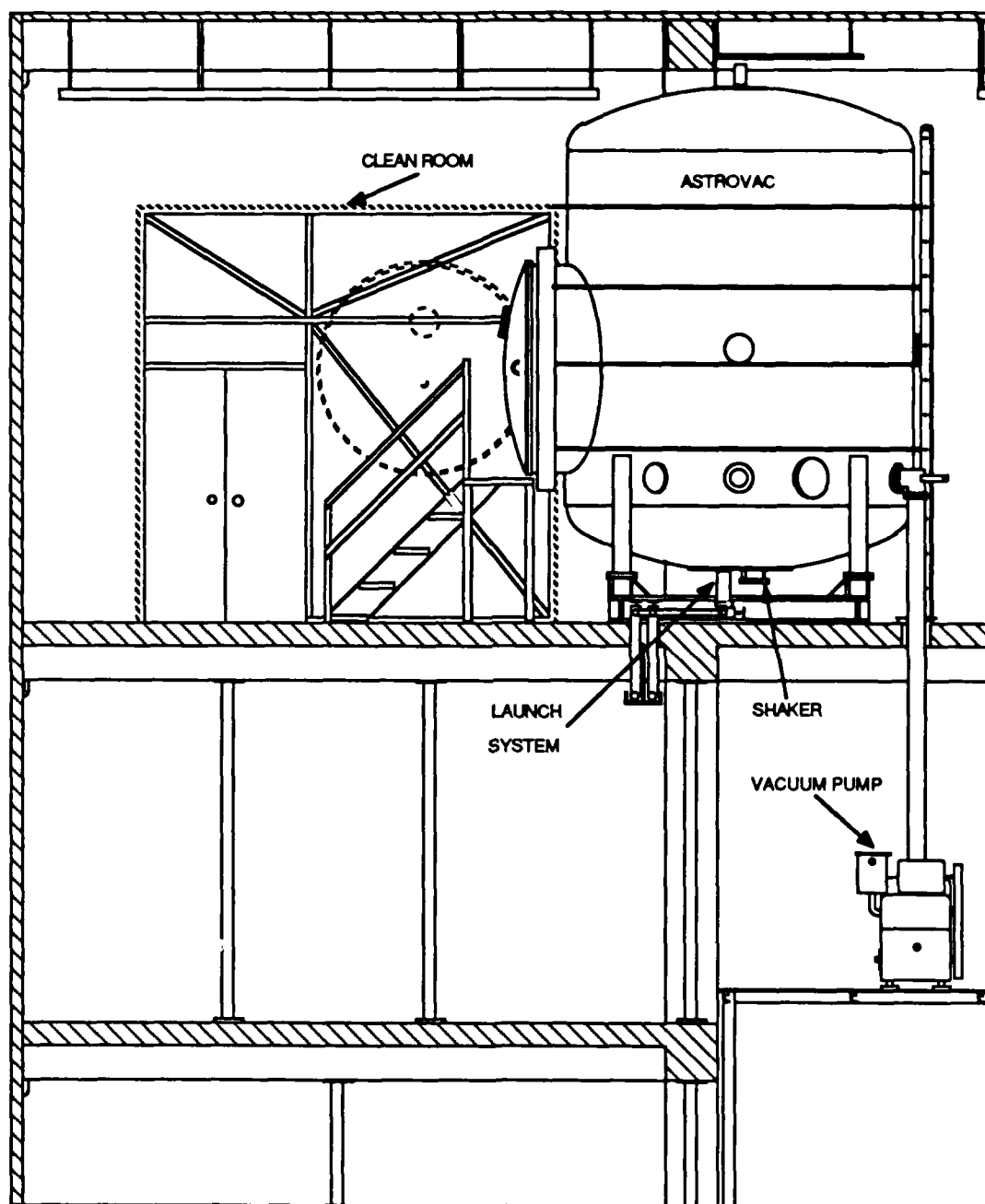


Figure 1. Overall Layout of the ASTROVAC Facility.

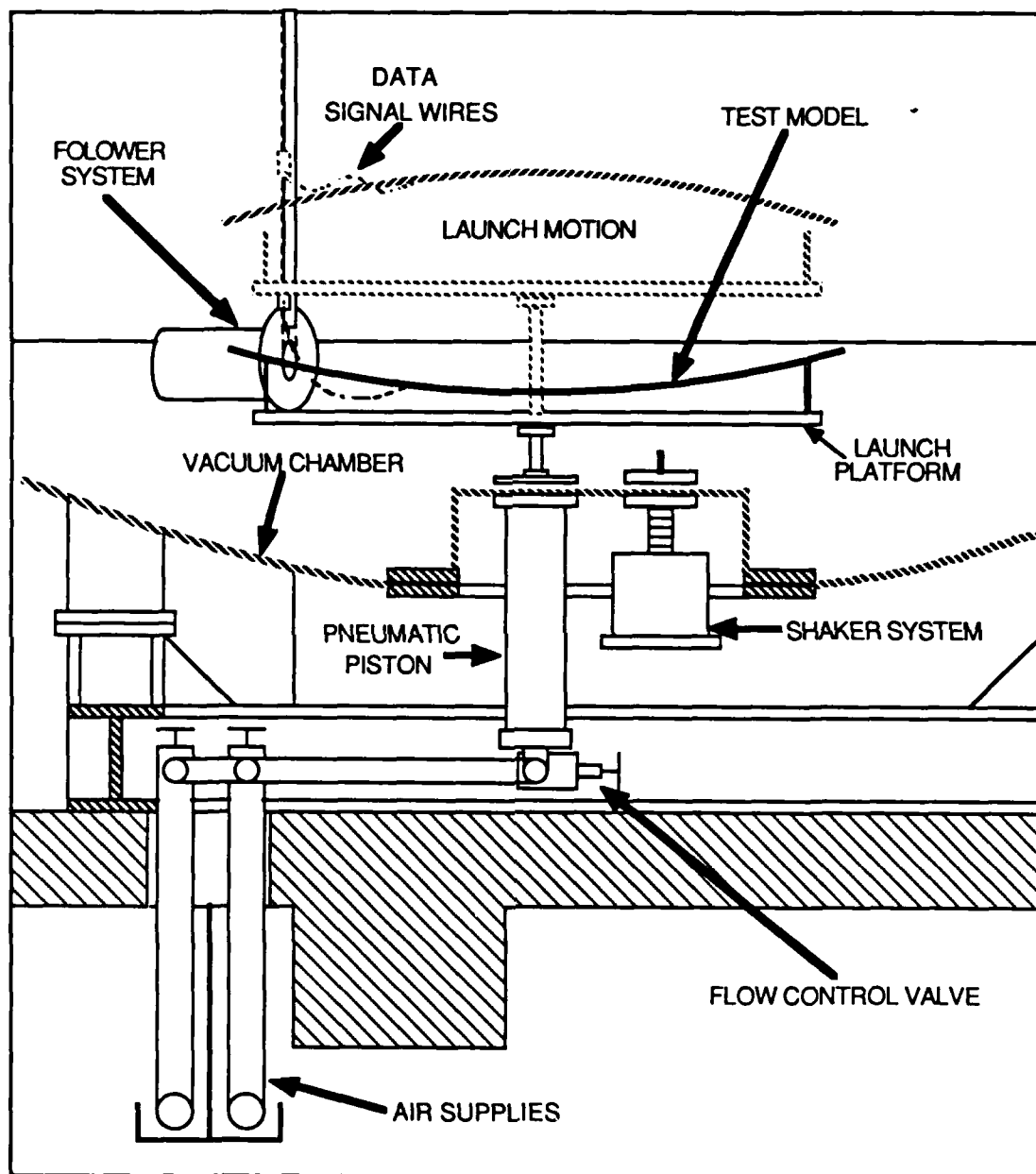


Figure 2. ASTROVAC Lofting System.

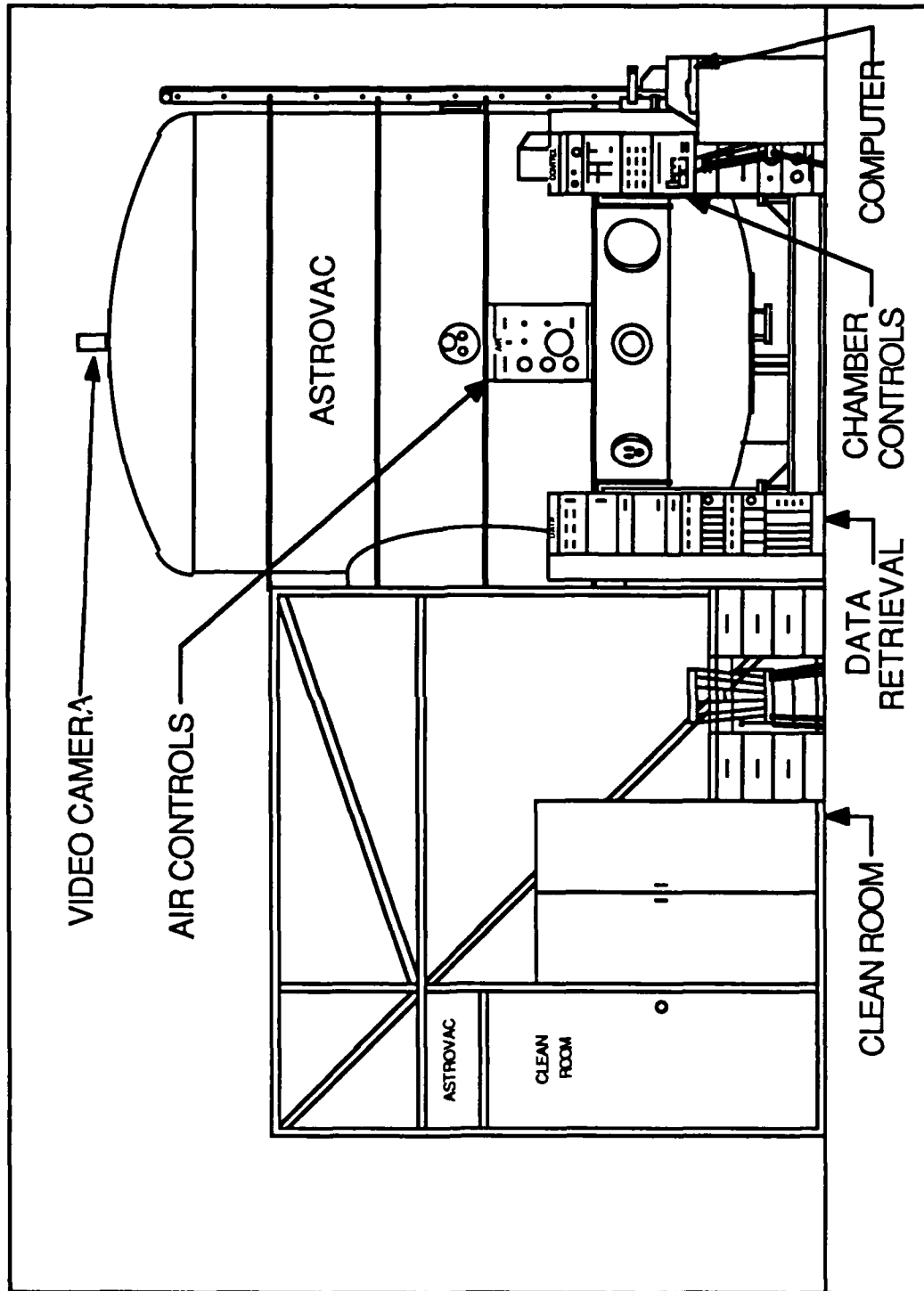


Figure 3. Data and Control System.

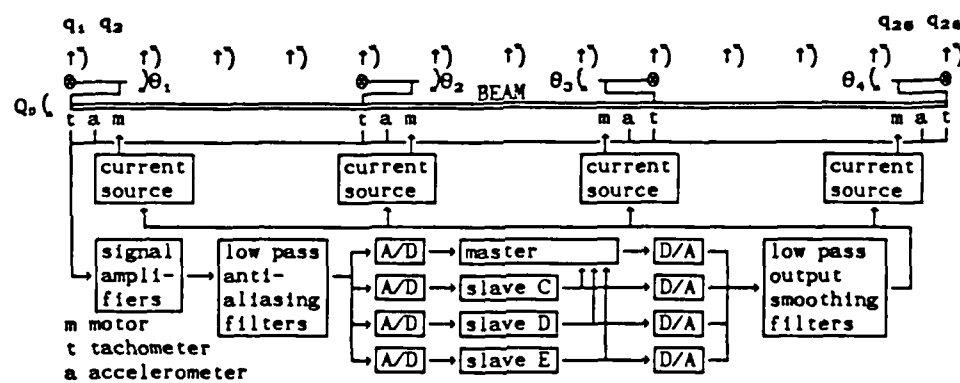


Figure 4. Equipment for the Control of Flexible Structures.

APPENDIX 1:

THEORETICAL AND EXPERIMENTAL INVESTIGATION OF  
SPACE-REALIZABLE INERTIAL ACTUATION  
FOR PASSIVE AND ACTIVE STRUCTURAL CONTROL

David W. Miller  
Research Assistant

Edward F. Crawley  
Associate Professor

Space Systems Laboratory  
Department of Aeronautics and Astronautics  
Massachusetts Institute of Technology

### Abstract

Inertial reaction devices are investigated for use as passive vibration absorbers and active control actuators for flexible space structures. Absorbers are designed for one and two degree of freedom structural representations using three parameter optimization techniques. All three yield nearly identical designs and indicate that inertial devices should be tuned to the lowest mode intended to receive increased damping. The optimal passive components of the control actuator are found to be those of the optimal passive vibration absorber. Proof of concept laboratory tests were performed on a quasi free-free beam using inertial reaction devices which are space-realizable, i.e. conceptually capable of functioning in the space environment. The inertial devices were used both as passive absorbers and as tuned actuators. Damping was significantly increased using both passive and passive/active techniques. Additional tests indicated the benefits and limitations of actuator tuning and the necessity of performing realistic experiments using space-realizable hardware.

### Nomenclature

A	= state dynamics matrix
$b_i$	= $i^{\text{th}}$ row of control effectiveness matrix
B	= control effectiveness matrix
c	= damper strength
$c_{i1}$	= $i^{\text{th}}$ column of modal measurement matrix
C	= regulated variable matrix
$d_i$	= $i^{\text{th}}$ row of modal disturbance matrix
D	= disturbance effectiveness matrix
$D_c$	= positive definite modal damping matrix
f	= feedback gains
F	= control force, feedback gain matrix
J	= system cost
$k_i$	= stiffness of $i^{\text{th}}$ spring
$m_i$	= mass of $i^{\text{th}}$ mass
M	= measurement matrix
P	= disturbance force
Q	= quadratic state penalty
$Q_0$	= disturbance torque
R	= quadratic control effort penalty
u	= nondimensional control force
w	= disturbance inputs
x	= state vector, displacement
y	= regulated variables
z	= measured variables
$\alpha$	= positive gain parameter
$\beta$	= absorber-to-structural modal mass ratio



- $\gamma$  = nondimensional frequency ratio
- $\delta$  = absorber-to-structure modal frequency ratio
- $\mu$  = nondimensional damper strength
- $\sigma_i$  = second-order modes for internally balanced system
- $\Phi_{DEC}$  = decimated eigenvector matrix
- $\zeta_i$  = damping of  $i^{th}$  mode
- $\omega_i$  = frequency of  $i^{th}$  mode

### Introduction

A number of future space structures may require active control of their flexible modes. Because of the lack of passive energy dissipation mechanisms in space, even small disturbances can lead to motions of sufficiently large amplitude or duration as to be detrimental to performance requirements. A two level approach to controlling structural vibrations is envisioned. First, the background structural and material damping can be increased by addition of passive damping devices. Second, an active control system can be added to further enhance system performance. In this scenario, the purpose of the passive damping device is threefold: to provide a supplementary passive dissipation mechanism; to increase the robustness of the active system; and to provide a fall back in the event of failure of some or all of the active system.

Several options are available for introducing passive damping and active control into the structural dynamics. Passive energy dissipation mechanisms which can be implemented in space include: material damping enhancement, viscoelastic dampers, frictional dampers and joints, intermember dampers, and inertial reaction absorbers. Mechanisms for active damping include: piezoelectric devices, interelement actuators, angular momentum exchange devices, and inertial reaction actuators. Common to the list of options for passive dissipators and active actuators are inertial reaction devices. These

are conceptually simple devices that are easily implemented in space. Questions associated with such devices include their theoretical optimization and experimental implementation.

Previous investigations have addressed theoretical optimization of passive absorber designs. The classical single degree of freedom (DOF) vibration absorber solution<sup>1</sup> is well known and has found wide application. Recently, a closed form solution was derived, based on a quadratic regulator formulation, that yields the same design for a one DOF absorber.<sup>2</sup> Currently, these devices are commonly used to damp structures which respond primarily in a single mode of vibration. This work will extend their application to the damping of two DOF structures, and will examine their performance in structures with multiple modes. The incorporation of vibration absorbers as the passive components of active inertial control actuators will also be examined.

Inertial reaction actuators are conceptually capable of functioning in the space environment; i.e., they are space-realizable. One practical implementation of an inertial reaction actuator is the pivoted proof-mass actuator, currently being considered for use in active vibration suppression.<sup>3 4</sup>

<sup>5</sup> The work presented here makes use of similar devices, but incorporates tunable passive components into the design of active control actuators for the implementation of low authority control<sup>4</sup>. A distinction of the experiments described below is that no actuating or sensing is performed against the laboratory frame. This work focuses on the use of tunable inertial reaction devices, which operate through momentum exchange between the structure and a reaction mass, to perform output feedback control.<sup>6</sup>

This paper is divided into two main sections which deal with the issues of theoretical optimization and experimental implementation. First, the components of a passive inertial vibration absorber and the passive components of an

inertial control actuator are optimized. The passive absorber (Fig. 1a) consists of a spring, mass, and damper. With the addition of a feedback control force  $F$  in parallel, the device becomes an active control actuator. Because of the functional similarities in the inertial absorber and actuator models, both concepts can be combined into one physical device. The availability of adjustable passive parameters allows the passive and active characteristics of the actuator to complement each other. The absorber and actuator are optimized by several criteria including minimum steady-state response, minimum modal time constant, and quadratic cost minimization.

In the second part of this paper, experiments are used to identify practical approaches and limitations in the use of these devices. First, the actuators are experimentally tuned to beam modes as absorbers. Once tuned, these devices are used as control actuators. A control test is performed using actuators without optimized passive characteristics in order to demonstrate that improved performance is achieved when the actuators are tuned. Finally, a test involving actuation against the laboratory frame is used to demonstrate the relative ease in gaining deceptively high performance with a nonspace-realizable devices.

#### Optimization of Passive Absorber Parameters

The passive inertial vibration absorbers are first optimized for the systems shown in Fig. 1. In Fig. 1b the absorber ( $m_2$ ,  $k_2$ , and  $c$ ) is attached to a single degree of freedom spring/mass system ( $m_1$  and  $k_1$ ) which represents the modal stiffness and modal mass of one structural mode. Fig. 1c is the model used for optimizing the absorber to a two DOF plant. The force  $P$  indicates the location of an assumed input disturbance on the structure.

Three different approaches are used to determine the optimal spring and damper values for the passive vibration absorber. First, a steady-state minimax

criterion is used to select parameters that minimize the maximum steady-state structural response. Second, a set of absorber parameters is chosen which places the system poles such that the maximum modal time constant is minimized. A third optimal solution is found by minimizing a weighted quadratic cost integral of the response. The steady-state minimax criterion is then extended to the selection of optimal absorber parameters for damping two DOF systems. Finally, the minimum cost' criterion is applied to the simultaneous and sequential optimizations of the passive components of an actuator and the active feedback gains.

#### Optimal Absorber Design for a One DOF Structure

Steady-State Solution. The first optimality criterion is to minimize the maximum steady-state response  $x_1$  when the structural mass  $m_1$  is subjected to a white noise disturbance  $P$ . The nondimensional transfer function relating input disturbance to response for the model in Fig. 1b is

$$\left| \frac{x_1}{P/k_1} \right|^2 = \frac{4\mu^2\gamma^2 + (\gamma^2 - \delta^2)^2}{[\beta\delta^2\gamma^2 - (\gamma^2 - 1)(\gamma^2 - \delta^2)]^2 + 4\mu^2\gamma^2[\gamma^2(1 + \beta) - 1]^2} \quad (1)$$

where

$$\delta = [(k_2/m_2)/(k_1/m_1)]^{1/2} \text{ absorber/structure frequency ratio} \quad (2a)$$

$$\gamma = \omega/(k_1/m_1)^{1/2} \text{ nondimensional frequency ratio} \quad (2b)$$

$$\beta = m_2/m_1 \text{ absorber/structure mass ratio} \quad (2c)$$

$$\mu = c/2m_2(k_1/m_1)^{1/2} \text{ nondimensional damping} \quad (2d)$$

The solution based upon minimization of the maximum steady-state response, known as the "Classical Vibration Absorber" problem,<sup>1</sup> is summarized here. The maximum response of the structural mass  $m_1$  with an optimally tuned absorber attached is

$$\left| \frac{x_1}{P/k_1} \right|_{\max} = \left[ \frac{2 + \beta}{\beta} \right]^{1/2} \quad (3)$$

It is clear that increasing the absorber/structure mass ratio  $\beta$  lowers the response. Therefore, increasing the absorber mass improves performance and no "optimal" mass ratio exists. Therefore, the mass ratio  $\beta$  is assumed fixed and the values of the frequency ratio  $\delta$  and nondimensional damper  $\mu$  are optimized.

For a fixed mass ratio, the optimal frequency ratio  $\delta_{ss}$ , based on the minimax criterion is

$$\delta_{ss} = 1/(1 + \beta) \quad (4)$$

and the optimal nondimensional damper setting is found by solving

$$\mu_{ss}^2 = \frac{(\delta_{ss}^2 - \gamma_{ss}^2)^2 - [\beta \delta_{ss}^2 \gamma_{ss}^2 - (\gamma_{ss}^2 - 1)(\gamma_{ss}^2 - \delta_{ss}^2)]^2 (X_1 k_1 / P)^2}{4 \gamma_{ss}^2 (\gamma_{ss}^2 (1 + \beta) - 1)^2 (X_1 k_1 / P)^2 - 4 \gamma_{ss}^2} \quad (5)$$

where the nondimensional modal frequencies are

$$\gamma_{ss}^2 = \frac{1}{1 + \beta} \left[ 1 \pm \left[ \frac{\beta}{2 + \beta} \right]^{1/2} \right] \quad (6)$$

Equation 5 is indeterminate at these modal frequencies  $\gamma_{ss}$ . To determine  $\mu_{ss}$ , a limit of Eq. 5 must be taken for values of  $\gamma$  approaching  $\gamma_{ss}$ .

A numerical example of this steady-state solution is shown in Fig. 2 for a mass ratio of  $\beta = 0.02$  (i.e., the absorber mass  $m_2$  is 2% of the structural modal mass  $m_1$ ) and for the optimal frequency ratio of  $\delta_{ss} = 0.98$ . Given this mass and frequency ratio, Fig. 2 shows the response to white noise excitation for six nondimensional damper settings. Notice that  $\mu = 0.086$  appears to minimize the maximum response, and in fact corresponds to  $\mu_{ss}$  derived using Eq. 5.

Transient Response Solution. The criterion used to determine the optimal transient response solution is that of minimizing the maximum modal time constant. Fig. 3 shows the root locus for the system of Fig. 1b as the damper  $\mu$  is varied (for a mass ratio of  $\beta = 0.02$ ). The frequency ratio  $\delta$  has been chosen such that the root trajectories intersect at point A. This allows both poles to be moved as far to the left as possible. This optimal value of  $\delta_{tr}$  which causes the loci to intersect at point A is the same as that calculated using Eq. 4.

The optimal damping that places both poles at point A is

$$\mu_{TR}^2 = \beta / (1 + \beta)^3 \quad (7)$$

The real part of the poles at point A is

$$\text{RE}(s) \Big|_A = -0.5 [ \beta / (1 + \beta) ]^{1/2} \quad (8)$$

As in the steady-state response optimization, optimum performance improves monotonically for increasing  $\beta$ . For the numerical example of  $\beta = 0.02$ ,  $\delta_{ss} = \delta_{TR} = 0.98$  (Eq. 4), the optimal damper is  $\mu_{TR} = 0.137$  (Eq. 7), which is 60% larger than the value for  $\mu_{ss}$  derived using the steady-state minimax criterion (Eq. 5). Figure 3 also shows the pole locations for the system with the optimal steady state response (  $\delta = \delta_{ss} = \delta_{TR}$  and  $\mu = \mu_{ss}$  ). In general, lower damping is required for optimal steady state response than for optimal transient response.

Minimum Quadratic Cost Solution. The final optimality criterion for passive absorbers is to minimize a cost function that penalizes the undesirable system response. To be consistent with optimal regulator theory, the quadratic cost function is

$$J = \frac{1}{2} \int_0^{\infty} [ x^T Q x + u^T R u ] dt \quad (9)$$

where  $x$  contains the states of the system of Fig. 1b, and  $Q$  is a positive semi-definite square matrix. In this problem there are no active forces, so that the cost depends only on the quadratic of  $x$ , i. e.  $R = 0$ . For a given  $Q$  and initial state vector  $x_0$ , a unique solution for a minimum of  $J$  can be found by solving the Lyapunov equation for the system.<sup>7</sup> A closed form analytic solution for this problem has been found for the case of a vibration absorber attached to a one DOF system.<sup>2</sup> This solution yields the same optimal frequency ratio  $\delta_{ss}$  and a similar damping level  $\mu$  as was found above for the steady-state optimization.

For this analysis, a numerical search is used to determine the values of frequency ratio  $\delta$  and nondimensional damper  $\mu$  which result in the lowest cost  $J$  for a fixed mass ratio  $\beta$ . The weighting matrix  $Q$  is selected so that the cost  $J$  represents the sum of the system's total nondimensional kinetic plus potential energy. Choice of the initial condition  $x_0$  does not significantly affect the results for a lightly damped system.

Optimal solutions using the three methods were compared<sup>8</sup> and found to have identical frequency ratios and similar nondimensional dampers. Thus, all three design techniques yield virtually identical absorber designs, particularly with respect to achievable tuning accuracy of these devices.

#### Optimal Absorber Design for a Two DOF System.

The possibilities of adding damping to several modes through the use of a single absorber is demonstrated by extending the steady-state solution to the design of an absorber for a two DOF structure (Fig. 1c). Once again, the objective is to minimize the maximum steady-state response at the disturbance location. For a structure with multiple DOFs, no simple closed form solution, such as Eqs. 4 and 5, is known. A nonrigorous extension of the single DOF absorber analysis is presented.

The optimization possibilities are summarized in Fig. 4 where the frequency response of the system in Fig. 1c is shown for two sets of passive absorber parameters. Again, the mass ratio is fixed at  $\beta = 0.02$  where  $\beta$  is now defined as the ratio of absorber mass to the modal mass of the lower structural mode. Curve 1 shows the absorber tuned to the lower structural mode using the relations given in Eqs. 4 and 5 altered to refer to modal properties. In this case the absorber parameters yield a suboptimal result because the response at the high mode frequency is about four times larger than the response of the lower two modes. Increased absorber damper strength reduces apparent damping in

the lower two modes while increasing residual damping in the high mode. The term "apparent damping" refers to the damping exhibited by the combined steady-state response of two split modes which occur at almost identical frequencies. With sufficient additional damping the two peak magnitudes are equated and the minimax criterion is again satisfied (Curve 2).

The absorber frequency can also be tuned to the higher structural mode. However, this choice of absorber frequency is inappropriate. When the absorber frequency is tuned to the higher mode, no value of the damper can be found which equates the response of the two structural modes. It is therefore important that, when attempting to introduce significant levels of damping into more than one structural mode, the absorber frequency should be tuned to the frequency of the lowest mode of interest and the damper increased from the value determined by Eq. 5 until the desired damping in the higher modes is achieved. The validity of this approach was independently confirmed by a quadratic cost minimization approach.<sup>8</sup>

#### Optimization of Passive Components of an Active Actuator.

The next step in the study of inertial reaction devices is to determine the optimal passive components of the active control actuator shown in Fig. 1a. The control force  $F$  is assumed to be a linear function of the displacement and velocity states of both the structural mass  $m_1$  and the actuator  $m_2$  of Fig. 1b; i.e., full state feedback. Both the active feedback gains and the values of the passive components are optimized simultaneously. The objective of this optimization is to determine what similarity these passive parameters bear to the optimal parameters of the passive vibration absorber.

The method used for the simultaneous optimization of the active feedback gains and passive parameters is similar to the previously discussed quadratic cost minimization (Eq. 9). The quadratic cost now includes a penalty on the



control effort, so that  $R$  is a positive, dimensionless constant. By the choice of  $R=100$ , the level of control forces are kept to the same order of magnitude as those generated by the passive components. This is done to prevent domination of the actuator dynamics by either the passive components or active forces. Since a tuned absorber provides significant passive damping in the tuned mode, at a relatively low mass ratio, the addition of active control forces of the same order of magnitude would provide damping performance well within the level necessary for typical applications.

To simultaneously optimize the passive components and active gains, a gradient search is performed for a range of values of the actuator's passive frequency ratio  $\delta$  and nondimensional damper  $\mu$ . For each  $\delta$  and  $\mu$ , the optimal regulator gains are calculated exactly from regulator theory and the cost (Eq. 9) evaluated. Note that no penalty is explicitly placed on the passive components, and therefore the optimal solution will be driven towards relying as heavily as possible on the passive components of the actuator.

The two systems that were optimized for the passive vibration absorber (Figs. 1b and 1c) were also optimized for the active actuator<sup>8</sup>. One characteristic result throughout the optimizations was that the optimal  $\delta$  for the actuator is near the optimal  $\delta_s$  of the passive vibration absorber. The optimal value of the damper  $\mu$  is somewhat more sensitive to the presence of active feedback and therefore deviates from the optimal for an absorber by a greater percentage than do the frequency ratios.

The results of the simultaneous optimization suggest that sequentially optimizing first the passive components and then the active gains will yield nearly the same performance. This indicates that the inertial reaction control actuator performs most effectively when passively tuned as a vibration absorber. Supplemental passive damping is added to the system, and actuation effectiveness

is increased.

### Experiments Using Inertial Reaction Control Actuators

In order to investigate the practical implementation and limitations of space-realizable active control, an extensive set of experiments was conducted. The experimental objective was to maximize the damping in a pendulous free-free beam. After a description of the experimental hardware and open-loop plant model, the results for the test in which the inertial reaction devices were experimentally tuned as passive vibration absorbers to various beam modes are discussed. Once tuned, these devices were used as active actuators through the feedback of system measurements. Finally, the performance of these controllers is compared to the performance of untuned and nonspace-realizable actuators.

#### Experimental Apparatus.

Control Hardware. The structural plant of a prototypical space structure can be characterized as having free boundary conditions and a low frequency fundamental mode. Such conditions raise issues concerning actuator stroke limitations and low frequency stiction effects. This behavior was simulated by a twenty-four foot brass beam, suspended by wires arranged in six sets of swinging parallelograms (Fig. 5a), which prohibited torsional rotation about the beam's longitudinal axis. The first bending mode of this free-free structure was at 0.37 Hz. The pendulous modes were at 0.30 Hz and 0.32 Hz. The small frequency separation between the pendulous and first bending modes was due to a desire to make the flexible modes as low as possible and a restriction on the suspension length. The system had four modes below 1.0 Hz. and twelve modes below 10.0 Hz (Table 1) providing the experimental challenge of close modal spacing. Typical open-loop modal damping ratios averaged 0.16% of critical ( $\zeta = 0.0016$ ).

Four identical space-realizable Electromagnetic, Inertial-Reaction

Actuators, with characteristics as listed in Table 2, were used to control the structure (Fig. 5b). These devices, which are variations of devices developed at the Lockheed Palo Alto Research Laboratory,<sup>3</sup> are attached to the side of the beam and use a commanded motor torque to accelerate a pivoting reaction arm through small angle deflections. This causes the proof-mass, attached to the end of the pivoting arm, to accelerate horizontally in a direction transverse to the beam. At the point of attachment of the actuator to the beam, this motion generates a reaction force and a small reaction torque, both of which must be modeled.<sup>9</sup> An adjustable spring was included to enable adjustment of the natural frequency of each device, and colocated feedback of motor shaft rate to motor torque was locally fed back to simulate a passive damper, thus allowing the devices to be used as both tunable vibration absorbers and control actuators with tunable passive components. The active damper provided simple damping adjustment and linearity. In principle, it could be replaced with a truly passive mechanism such as constrained viscoelastic layers in the adjustable spring. For the remainder of this paper, the adjustable spring and locally fed back colocated, electronic damper will be referred to as passive elements of the device. A momentum wheel was attached to one end of the beam to provide either broadband disturbance torque used in transfer function tests, or sinusoidal disturbance torques used to initiate free decay tests.

Eight space-realizable sensors were used to estimate system states. Each actuator contained a tachometer for measuring relative reaction arm rotation rate. At the location of each actuator, an accelerometer was used to measure coincident inertial beam acceleration. The beam and actuator positions and velocities at each actuator location were estimated from the tachometer and accelerometer measurements by a digital algorithm which filters low frequency signal drift and integrates the measurements over a frequency range encompassing

the system modes of interest<sup>9</sup>.

Discrete time processing was accomplished in one master and three slave 8088/8087 processors with each of the four processors devoted to controlling a separate actuator. Measurement information was exchanged between processors through dual access, shared memory space. Analog-to-digital and digital-to-analog conversion was used by each processor for sensor sampling and issuing control commands at a rate of 1000 Hz. This high control rate allowed feedback gains to be derived based on the assumption of continuous control for modes up to 10 Hz. Double precision operations were used to prevent roundoff errors in the integration and control algorithms. The details of the digital hardware are listed in Table 3. Once this equipment was assembled as illustrated in Fig. 6, a mathematical model of the system was constructed and verified.

System Model. A finite element model, consisting of twelve cubic beam elements and augmented by the dynamics of the four actuators, was formulated using the DOFs indicated in Fig. 6. The model was first formulated with only the twenty-six beam degrees of freedom, plus the mass and disturbance torque  $Q_0$  of the momentum wheel, and the stiffness of the suspension system. Very slight changes in the beam cross sectional stiffness were made so that this model accurately represented the experimentally observed open-loop beam behavior. Then the actuators, with springs set very stiff, were physically added to the beam and mathematically added to the model. Modal damping was then experimentally determined for each mode and added to complete the mathematical model of the form

$$\begin{aligned}
 & \left[ \begin{array}{ccc} & & 0 \\ & F & \\ & E & \\ 0 & & M \end{array} \right]_{26 \times 26} \begin{bmatrix} \ddot{q}_1 \\ \vdots \\ \ddot{q}_{26} \\ \ddot{\theta}_1 \\ \vdots \\ \ddot{\theta}_4 \end{bmatrix}_{30 \times 1} + \left[ \begin{array}{ccc} & & 0 \\ & F & \\ & E & \\ 0 & & M \end{array} \right]_{26 \times 26} \begin{bmatrix} \dot{q}_1 \\ \vdots \\ \dot{q}_{26} \\ \dot{\theta}_1 \\ \vdots \\ \dot{\theta}_4 \end{bmatrix}_{30 \times 1} \\
 & \quad \text{ACTUATOR DYNAMICS} \quad \text{ACTUATOR COUPLING TO BEAM} \quad \text{ACTUATOR DYNAMICS} \quad \text{ACTUATOR COUPLING TO BEAM} \\
 & \left[ \begin{array}{ccc} & & 0 \\ & F & \\ & E & \\ 0 & & M \end{array} \right]_{26 \times 26} \begin{bmatrix} q_1 \\ \vdots \\ q_{26} \\ \theta_1 \\ \vdots \\ \theta_4 \end{bmatrix}_{30 \times 1} = \begin{bmatrix} Q_1 \\ \vdots \\ Q_{26} \\ \tau_1 \\ \vdots \\ \tau_4 \end{bmatrix}_{30 \times 1} + \begin{bmatrix} 0 \\ Q_0 \\ 0 \\ \vdots \\ \vdots \\ 0 \end{bmatrix}_{30 \times 1} \quad (10) \\
 & \quad \text{ACTUATOR DYNAMICS} \quad \text{ACTUATOR COUPLING TO BEAM} \quad \text{ACTUATOR DYNAMICS} \quad \text{ACTUATOR COUPLING TO BEAM}
 \end{aligned}$$

With this refined model, the first seventeen predicted open-loop modal frequencies of the beam, plus stiff actuators, were within 2% of their measured values. The final actuator stiffnesses and damper strengths used in the model were determined during the actuator tuning process.

In each of the following experiments, two types of tests were performed. First, the acceleration transfer function from broadband disturbance torque at one end of the beam ( $Q_0 = 0.006$  Newton Meters RMS) to linear transverse beam acceleration at the other end was recorded via a spectrum analyzer. Second, the beam was excited at individual modal frequencies and allowed to undergo free decay after shutdown of the excitation while beam end acceleration was measured. The modal damping ratios were calculated from these transient decays.

#### Tuned Passive Absorber Experiments

The first set of experiments involved tuning the four actuators, used as passive absorbers, to four "target modes" of the beam, and determining their effectiveness as passive absorbers. Modes targeted for absorber tuning were those most sensitive to the disturbance. Equation 11 defines the modal transmission from disturbance to regulated variables for lightly damped systems

in the form of Eq. 12; as derived by internal balancing theory.<sup>10</sup> For this experiment, the regulated variables  $y$  have been chosen to be the entire state vector  $x$ ; i.e., it is desirable to minimize the disturbance to all of the physically scaled state variables equally. This selects the modes with the largest modal time constants.

$$\sigma_{bc_i}^2 = (4\zeta_i \omega_i)^{-1} [d_i d_i^T (\omega_i^{-2} + 1) c_i^T c_i]^{1/2} \quad (11)$$

$$\dot{x} = Ax + Bu + Dw \quad \text{state equation} \quad (12)$$

$$z = Mx \quad \text{measurement equation}$$

$$y = Cx \quad \text{regulated variable equation}$$

$$u = -Fz \quad \text{feedback equation}$$

In Eq. 11,  $\omega_i$  is modal frequency and  $\zeta_i$  is modal damping, and  $c_i$  and  $d_i$  are columns and rows of the regulated variable matrix  $C$  and disturbance matrix  $D$ , respectively.

Figure 7 shows with hatched bars the transmission, as defined by Equation 11, from the disturbance to the regulated variables for the first thirteen open-loop modes. The result of the analysis presented above, in which an absorber is tuned to more than one degree of freedom, indicates that it is desirable to tune to the lower frequency modes of interest. Therefore, the four lowest consecutive modes with high disturbance transmission were chosen as the target modes, as shown by the arrows in Figure 7. The four absorbers had been placed at positions along the beam where they exerted large influence on their respective modes due to large modal motion; i.e., the absorbers were placed in positions which maximized the modal mass ratio (Eq. 2c). One absorber was placed at each end and one was placed at each 1/3 length position (Fig. 5).

One absorber was tuned to each of the four target modes. The optimal passive absorber stiffness and damping were chosen using the steady-state minimax criterion (Eqs. 4 and 5). The mechanical spring in the actuator was

adjusted as accurately as possible to the optimal frequency, and colocated feedback of actuator rotational position and rate was used to fine tune the devices. While this does not result in a purely passive system, the active part was used only to enable easy tuning and was not necessary to the performance of the absorbers.

The performance and limitations of the four conceptually passive actuators were then assessed. A qualitative comparison of the acceleration transfer function of the beam is shown in Figure 8. Two traces are shown, one for the case of very stiff absorbers such that there is relatively little motion across the active dampers, and the second for the case of tuned absorbers. The four target modes are those with frequencies of 1.09, 1.74, 2.61, and 3.78 Hz. Note the reduced response (increased modal damping) in this frequency range as a result of absorber tuning. Additional, or residual damping is also evident in the modes above 4.0 Hz. The existence of residual damping in modes higher than the modes to which the absorbers are tuned is consistent with the observations made from the two DOF tuning analysis (Fig. 4).

The second set of tests involved transient decays of the target modes, the results of which are summarized in Table 4. As can be seen, by comparison of the modal damping ratios before and after tuning, over an order of magnitude increase in critical damping ratio was achieved. Sixty to ninety percent of the predicted damping was obtained. Due to the second-order dynamics of the absorbers, tuning to a target mode results in two split modes close in frequency to the original target mode frequency (e.g., target mode 5 becomes modes 5a and 5b). The damping ratio of the more lightly damped mode is reported in Table 4. The deviation between actual and predicted damping in target mode five was due to friction effects. Stiction would seize the actuator motion at low vibration levels causing marked reductions in damping and limiting low amplitude

performance. The low performance in mode eight was due to the low mass ratio which increases tuning sensitivity and difficulty. In general, the absorbers could not be tuned to modes lower than 1 Hz. due to stiction problems and prohibitively large tuned absorber motion.

Several beneficial characteristics occur as a result of absorber tuning. Figure 7 shows that predicted modal disturbance transmissions are significantly reduced (Eq. 11) for the beam with tuned absorbers (solid bars) when compared to those for the beam without the absorbers tuned (hatched bars). Due to split mode behavior, two solid bars occur for each of the four hatched bars corresponding to the original target modes 5 through 8.

Controllability of the target modes is also enhanced by tuning (Fig. 9). The modal control transmission from actuator to regulated variables is defined by internal balancing theory,<sup>10</sup> in a fashion similar to disturbance transmission, as

$$\sigma_{tc}^2 = (4[\omega_i]^{-1} [b_i b_i^T (\omega_i^{-2} + 1) c_{ii}^T c_{ii}])^{1/2} \quad (13)$$

The vector  $b_i$  corresponds to a row of the control effectiveness matrix  $B$ . Since these values indicate the effect of control action on the states of the system, they are good indicators of relative modal controllability. Note that the split target modes are most controllable. The next most controllable modes are the beam modes above the target modes. Modes lower than the target modes are relatively uncontrollable.

Significant increases in passive damping have been achieved by the addition of the passive absorbers. If these same devices are also used as active actuators, it can be argued that the damping is introduced with no additional mass penalty. While the benefits of adding passive absorbers are substantial, the limitations are also important. Friction poses a problem in damping low level vibrations where stiction can seize absorber motion. This might be



overcome with a high frequency torque dither, which might excite unwanted high frequency response, or through bearing improvement. Stroke limitations hinder tuning to low frequency modes at low mass ratios. Finally, passive tuning of the absorbers requires a precise knowledge of the target mode frequency.

#### Active Control Experiments

Once the actuators had been passively tuned as absorbers to the four target modes, three sets of control experiments were performed using negative output feedback (Eq. 12). First, dual rotational rate feedback was used to drive the DC motors of the four tuned actuators from the four tachometers using a fully populated, positive definite gain matrix  $F$ . Dual feedback refers like sensor to like actuator feedback (rotational shaft rate to shaft torque) where each sensor is physically located with an actuator.<sup>6</sup> In the second set of tests, the same dual measurements were fed back to untuned, zero stiffness actuators. This verified the effectiveness of tuning the actuators as absorbers with nonzero stiffness. Finally, a control test was performed using one actuator reacting against the laboratory frame. This demonstrates the performance differences between space-realizable and nonspace-realizable experiments.

Dual Feedback to Tuned Actuators. Two different tests were performed using positive definite, dual feedback as derived using the technique described in Reference 6. In this technique, a matrix  $D_c$  is chosen to be a positive definite, diagonal matrix whose entries are the desired increases in damping for a chosen set of modes equal in number to the number of actuators used. In this experiment, equal damping was desired such that  $D_c = \alpha I$ . Next, the modal eigenvector matrix of the full system model is decimated while retaining rows corresponding to actuator motion and columns corresponding to the chosen set of modes. This decimated matrix is designated as  $\Phi_{orc}$ . The feedback gain matrix is then derived as

$$F = \Phi_{DEC}^T D_c \Phi_{DEC}^{-1} \quad (14)$$

The quadratic form of Eq. 14 guarantees a positive definite feedback matrix.

The two tests that were performed differed in the four modes chosen to form  $\Phi_{DEC}$ . The first test used the lowest two target modes, to which actuators were tuned, and their two corresponding split actuator modes (5a, 5b, 6a, and 6b) to create  $\Phi_{DEC}$ . The second test used the first four beam modes above the target modes (modes 9, 10, 11, and 12) to create  $\Phi_{DEC}$ .

When the lowest two target and their corresponding actuator modes were chosen to derive the feedback through Equation 14, a feedback matrix resulted which contained highly nonuniform entries. This was due to the relatively large eigenvector entries corresponding to the motion of the two actuators tuned to these two lower target modes (5 and 6). The inversion of the decimated eigenvector matrix  $\Phi_{DEC}$  in Eq. 14 resulted in high feedback gains for the two actuators not tuned to these two lower target modes (i.e., the actuators tuned to modes 7 and 8). The highest gain loop was colocated feedback to the actuator which had been tuned to target mode eight. This gain was four orders of magnitude larger than the colocated feedback to the actuator tuned to target mode five. Because of the nonuniform gain matrix, this design only created significant feedback to actuators tuned to the higher two target modes (7 and 8).

Using this feedback, only minor increases in damping in modes 9 and 10 (at 4.95 and 6.42 Hz.) above the target modes occurred at the expense of damping in target mode eight (at 3.78 Hz.) of the beam/actuator system. Table 5 lists measured and predicted closed-loop modal characteristics for this test for the feedback gain level chosen. The model and the data are in fair agreement. This behavior can be explained using Fig. 3 to represent the root locus in the vicinity of mode eight. Above a certain level of positive colocated rate

feedback, that which places the poles at the equivalent of point A, one of the root trajectories for modes 8a and 8b moves towards the imaginary axis. This results in reduced apparent damping in that mode. Recall that the collocated rate feedback to the actuators tuned to modes 7 and 8 dominate the feedback gain matrix. The model did not predict reductions in modal damping, due to the feedback, at this gain level but did so at a slightly higher gain level.

An important limitation was realized through this test. The feedback used was at a level just below that which caused onset of a high frequency (67 Hz.) instrumentation/actuator instability, similar in nature to those reported in Reference 4. Only relatively low control performance was achieved prior to the onset of this instability. Due to the nonuniform gain matrix, the relatively high gains to one actuator caused a local instability before significant control authority could be exerted overall. The corrective step was to create a more uniform feedback matrix, while retaining the desirable positive definite, dual feedback properties.

In the second test with dual feedback to tuned actuators, Eq. 14 was again used to derive a feedback matrix using an eigenvector transformation  $\Phi_{DEC}$  based on the first four beam modes above the target modes (i.e., modes 9, 10, 11, and 12). Uniformity in the gain matrix was achieved since the actuator eigenvector entries were of similar magnitudes. Figure 10 compares the acceleration transfer function of the beam with only the tuned absorbers (a) to that of the beam with additional uniform feedback to tuned actuators (b). Significant increases in damping in modes 9 through 12 resulted at a cost of only slight reductions in apparent damping in target modes 5 through 8 (note the hatching in Fig. 10). Table 5 lists the predicted and measured modal characteristics. As can be seen in both Fig. 10 and Table 5, modes 9 and 10 received the largest increases in damping. Better performance was achieved in this case because all

four actuators were contributing evenly. In fact, all modes above 4 Hz. exhibited significant increases in damping. Again, an instrumentation/actuator instability limited the feedback gain level. This result verifies that uniform feedback provides better performance since it allows all actuators to contribute before the onset of instability.

Several conclusions can be drawn from this first set of two tests. Nonuniform feedback resulted in poor performance while uniform feedback allowed significant increases in higher mode damping at the slight sacrifice of modal damping in the target modes to which the actuators were tuned. The active feedback, while introducing additional damping, also redistributes the damping in the target modes across a wider spectrum. In both tests, positive definite dual feedback proved stable with respect to beam modes for all gain levels tested up to that which caused instrumentation/actuator instability. This type of feedback also guarantees an increase in total system damping but does not necessarily guarantee simultaneous damping increases in all modes at all gains.

Dual Feedback to Untuned Actuators. In the next set of experiments, the same type of dual rate feedback (Eq. 14) was used in conjunction with untuned, almost zero stiffness actuators. This was done to illustrate the benefits of tuning to plant modal frequencies in the range over which control is desired. As in the previous case, the feedback was increased until the onset of instrumentation/actuator instability. Table 6 lists the results for modes 5 through 12 at the highest stable gain level used. Note that the split modes associated with the dynamics of the actuators have now disappeared since the actuator stiffnesses have been set essentially to zero. The results in Table 6 verify, when compared to Table 5, that actuator tuning yields improved performance. To obtain the same response characteristics, a controller providing position and rate feedback would have to have active gains to the

untuned actuators that provide the passively generated reactions that exist in the tuned actuator case.

Nonspace-Realizable Actuation. The last test involved a nonspace-realizable method of control actuation in which one actuator reacted against the laboratory wall instead of the proof-mass at the end of the pivoting arm. In this case, simple colocated actuator rate was negatively fed back to the actuator. Figure 11 compares the acceleration transfer function of the beam with tuned absorbers (a) to that of the beam with one actuator allowed to react against the laboratory frame (b), showing how effective this simple feedback is. The level of feedback was again limited by the instrumentation/actuator instability. As is evident from the data, this simple single actuator arrangement resulted in much better performance than any of the space-realizable methods, even those using four actuators, because the mass ratio is effectively infinite. This illustrates the need to conduct space-realizable experiments in order to identify important limitations which may be overlooked when performing nonspace-realizable tests such as this.

### Conclusions

Several conclusions can be drawn from the theoretical optimization of these inertial reaction devices. Three different optimization procedures yielded almost identical absorber designs providing confidence in the tuning process. In addition, the optimal passive components of the control actuator were found to be similar to those of the optimal absorber. This allows passive damping to be added without significant mass penalty. Finally, when using an inertial device to increase damping in several modes, it is desirable to tune the frequency of the device to the lowest mode and adjust the damping accordingly.

Experimentally, an inertial reaction device was used effectively as both a passive vibration absorber and a control actuator, passively tuned as an

absorber, verifying the results of the tuning analysis that stated that passive tuning complements active control. This dual purpose device resulted in a mass savings, increased modal controllability, and reduced target mode disturbance transmission. Additional passive damping increases gain margin for feedback systems that are conditionally stable and allows a form of passive damping enhancement in the event of control system failure. These space-realizable experiments were found to be important in determining performance limitations due to instrumentation instabilities, friction in relative motion actuators, and actuator saturation at low frequencies. In addition, nonspace-realizable tests exhibited excellent damping performance which emphasized the need to investigate the realistic implementation limitations of space-realizable techniques. Uniformity in the positive definite, dual feedback matrix allowed better performance before the onset of instrumentation/actuator instabilities because all actuators were able to exert maximum stable feedback.

While the experiments were not able to achieve damping levels needed in proposed space structures ( 10% critical damping) they did achieve almost half this level in the target modes and increased the damping in the higher modes by almost an order of magnitude. This is typical of the performance required of a low authority controller with respect to providing significant increases in damping across a frequency range exceeding the bandwidth of the high authority controller. The corresponding high authority controller could be implemented using other actuators or using these same devices given that the dual feedback restrictions set in this paper are relaxed.

#### Acknowledgments

This research was supported by the Air Force Office of Scientific Research with Dr. Anthony Amos serving as technical monitor.

#### References

1. Timoshenko, S., Young, D.H. and Weaver, W. Jr., Vibration Problems in Engineering, Fourth Edition, John Wiley and Sons, New York, 1974.
2. Juang, J., "Optimal Design of a Passive Vibration Absorber for a Truss Beam," J. Guidance, Control and Dynamics, Vol. 7 No.6, Nov.-Dec. 1984, p. 733.
3. Aubrun, J.N., Breakwell, J.A., Gupta, N.K., Lyons, M.G., Marguiles, G., ACOSS FIVE (Active Control of Space Structures) PHASE 1A, Lockheed Missiles & Space Co., Inc., Mar.80-Sept.81.
4. Aubrun, J.N., Marguiles, G., "Low-Authority Control Synthesis for Large Space Structures," Lockheed Palo Alto Research Laboratory, Contract Report on Contract NAS1-14887, May 1982.
5. Wang, B.P., Horner, G.C., and Pilkey, W., "Optimal Damping for the Vibration Control of a Two-Dimensional Structure," AIAA Paper 81-1845, Aug. 1981.
6. Skidmore, G.R., Hallauer, W.L., Jr., "Experimental-Theoretical Study of Active Damping with Dual Sensors and Actuators," AIAA Paper no. 85-1921-CP, AIAA Guidance and Control Conference, Aug. 1985.
7. Kwakernaak, H., Sivan, R., Linear Optimal Control Systems, Wiley-Interscience, New York, 1972.
8. Miller, D.W., Crawley, E.F., Ward, B.A., "Inertial Actuator Design for Maximum Passive and Active Energy Dissipation in Flexible Space Structures," AIAA Structural Dynamics and Materials Conference, Paper no. 85-0777, Apr. 1985.
9. Miller, D.W., "Finite Active Control Elements for Large Space Structures," Space Systems Laboratory Report # 6-85, Department of Aeronautics and Astronautics, M.I.T, Air Force Contract #F49620-83-K-0026, 1985.
10. Gregory, C.Z.Jr., "Reduction of Large Flexible Spacecraft Models Using

Internal Balancing Theory." Journal Guidance, Control and Dynamics, Vol.  
7, No. 6, Nov.-Dec. 1984.



Table 1. Brass Beam and Suspension Characteristics

Length	l = 7.315 meters
Width	b = 0.102 meters
Thickness	t = 0.003 meters
Mass Density / Unit Length	m = 4.12 kg/meter
Bending Stiffness	EI = 30.0185 N meter <sup>2</sup>
Suspension Cable Length	L = 2.450 meters

<u>Mode</u>	<u>Freq (Hz)</u>	<u>Damping Ratio</u>
1	0.300	-
2	0.320	-
3	0.368	0.0057
4	0.632	0.0032
5	1.120	0.0021
6	1.820	0.0018
7	2.760	0.0014
8	3.840	0.0016
9	5.200	0.0014
10	6.640	0.0015
11	8.320	0.0016
12	10.160	0.0017

Table 2. Force Actuator Specifications and Components.

Maximum Actuator Force	3.0	Nts.
Actuator Mass w/o Proof-Mass	0.550	Kgs.
Proof-Mass Mass	0.165	Kgs.
Arm Length	0.127	m.
Motor Peak Amperage	4.920	Amps.
Motor Peak Voltage	19.10	Volts
Torque Constant	35.70	mN m/Amp.
Peak Stall Torque	173.0	mN m.
DC Motor	Pittman Corp. Model # 7214	
Tachometer	Inland Motor Model # TG-0702	
Accelerometer	Endevco Piezoresistive Model # 2262-25	

Table 3 Digital Control Hardware

<b>Master System</b>		
Packaging:		LabTech
CPU:	JF Microsystems	Model 8759 8088/8087 8 Bit STD Bus
A/D:	Analog Devices	Model RTI-1260 8 Differential Channels +/- 10 Volts 12 Bit Conversion 25 $\mu$ sec Conversion Time
D/A:	Analog Devices	Model RTI-1262 4 Channels +/- 10 Volts 12 Bit Conversion 25 $\mu$ sec Settling Time
<b>Slave System</b>		
CPU:	Ziatech	Model ZT 8830 8088 8 Bit STD Bus
A/D:	Intel	Model iSBX 311 8 Differential Channels +/- 5 Volts 12 Bit Conversion 50 $\mu$ sec Conversion Time
D/A:	Intel	Model iSBX 328 8 Channels +/- 5 Volts 12 Bit Conversion 20 $\mu$ sec Settling Time
High Speed		
Math Board:	Intel	Model iSBX 331 FMUL 50 $\mu$ sec

Table 4. Experimental Results of Absorber Tuning.

	5	6	7	8
Target Mode Number:	5	6	7	8
Target Mode Frequency (Hz):	1.09	1.74	2.61	3.78
Absorber/Modal Mass Ratio:	0.033	0.011	0.018	0.004
Optimal Frequency Ratio:	0.968	0.990	0.983	0.996
Optimal Nondimensional Damper:	0.111	0.062	0.079	0.039
Predicted Critical Damping Ratio:	0.0637	0.0362	0.0470	0.0231
Measured Critical Damping Ratio:	0.0441	0.0320	0.0438	0.0136
% Achievement (measured/predicted)	69.2%	88.4%	93.2%	59.0%
Damping Ratio Prior to Tuning:	0.0021	0.0018	0.0014	0.0016
Increase in Critical Damping Ratio:	21	18	31	9

Table 5. Test Results for Nonuniform and Uniform, Positive Definite Dual Feedback to Tuned Actuators

Mode Number	Freq. (Hz)	$\zeta$ Open Loop (meas.)	[NONUNIFORM]		% meas. pred.	[UNIFORM]		% meas. pred.
			Closed Loop (pred.)	Closed Loop (meas.)		Closed Loop (pred.)	Closed Loop (meas.)	
5a	1.05	0.0441	0.0441	-----		CRIT	-----	
5b	1.27	-----	0.0479	-----		0.0233	-----	
6a	1.72	0.0320	0.0329	-----		0.8635	-----	
6b	1.88	-----	0.0382	-----		0.0470	-----	
7a	2.49	-----	0.0709	-----		0.7144	-----	
7b	2.75	0.0438	0.0715	-----		0.0546	-----	
8a	3.69	0.0136	CRIT	CRIT		0.4131	-----	
8b	3.95	-----	0.0173	0.0095	54.9%	0.0259	-----	
9	4.95	0.0040	0.0055	0.0110	200.0%	0.0155	0.0118	76.0%
10	6.42	0.0033	0.0042	0.0041	97.6%	0.0156	0.0129	83.0%
11	8.19	0.0048	0.0055	0.0047	85.5%	0.0103	0.0084	82.0%
12	9.80	0.0025	0.0029	0.0025	86.2%	0.0075	0.0060	80.0%
-----	not measured							

Table 6. Test Results for Uniform, Positive Definite Dual Feedback to Untuned (Zero Stiffness) Actuators.

Mode Number	Frequency (Hz)	Open Loop (measured)	Modal Closed Loop (predicted)	Damping Ratio Closed Loop (measured)	% Achievement <u>measured</u> / <u>predicted</u>
5	1.09	0.0021	0.0048	-----	
6	1.74	0.0018	0.0094	-----	
7	2.61	0.0014	0.0056	-----	
8	3.78	0.0016	0.0054	-----	
9	4.92	0.0014	0.0025	0.0018	72%
10	6.40	0.0015	0.0034	0.0031	91%
11	8.19	0.0016	0.0023	0.0017	74%
12	9.79	0.0017	0.0042	0.0030	71%
-----	not measured				

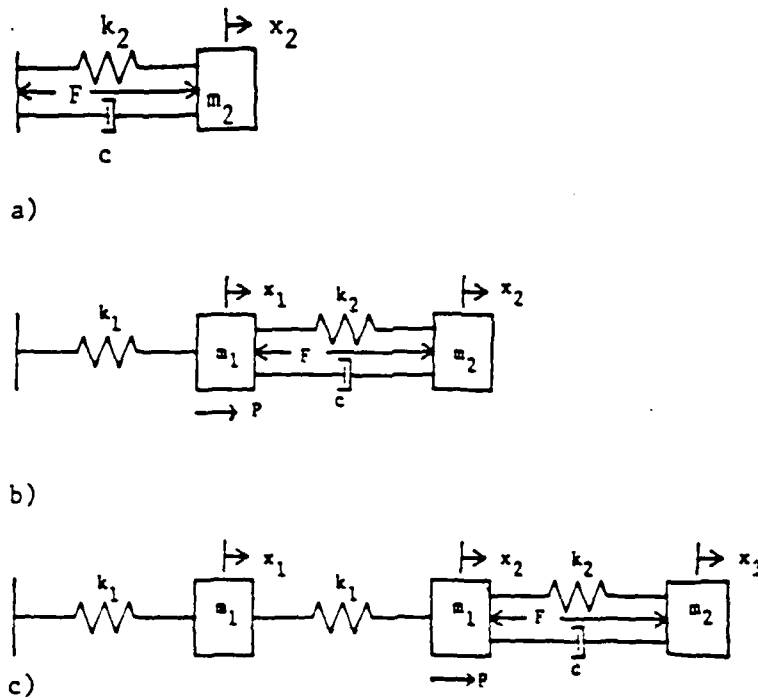


Figure 1 a) A One Degree of Freedom Absorber/Actuator Coupled to  
 b) a One DOF Structure and c) a Two DOF Structure.

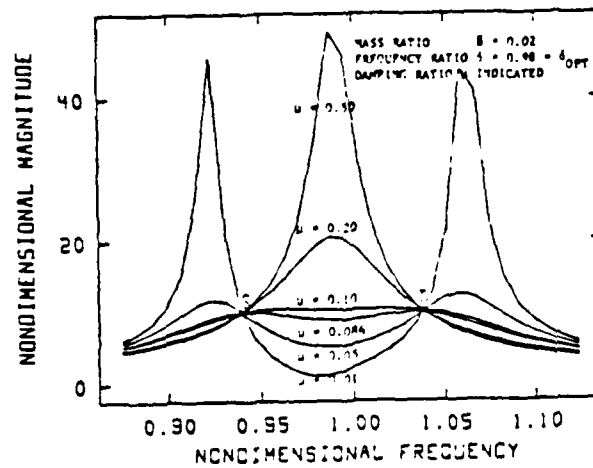


Figure 2 Response  $(x_1 k_1 / P)$  Versus Frequency  $(\omega / (k_1 / m_1)^{1/2})$  for the  
 System of Fig. 1b for the Optimal Frequency Ratio, the  
 Given Mass Ratio, and the Indicated Damping.

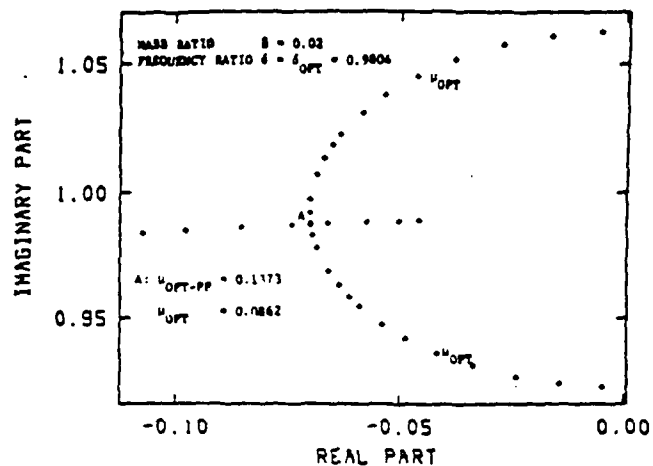


Figure 3 S-Plane Representation of the Poles of Figure 1b as a Function of Increasing Dumper Value.

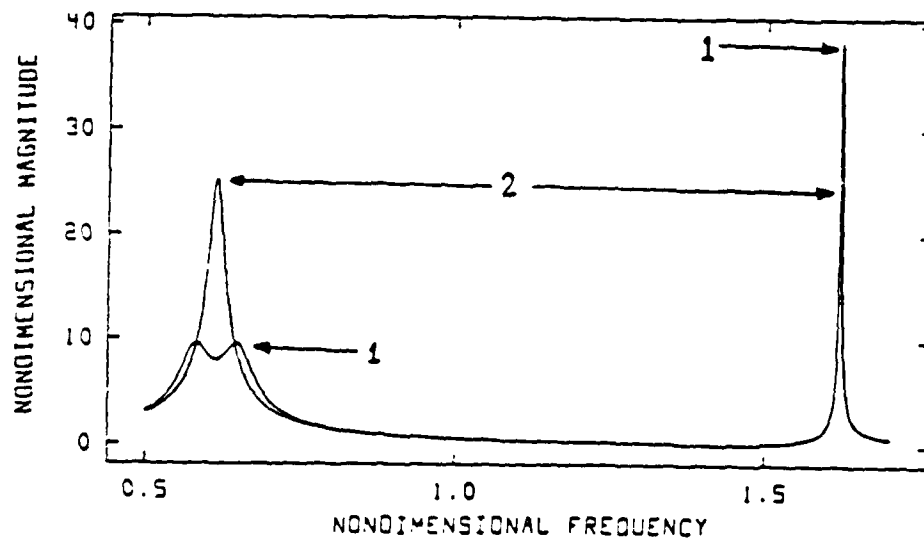


Figure 4 Response ( $x_1 k_1 / P$ ) Versus Frequency ( $\omega / (k_1 / m_1)^{1/2}$ ) for the System of Fig. 1c for the Choice of Damping Which Minimizes the Responses of the Lower Two Modes (Curve 1) and All Modes (Curve 2).

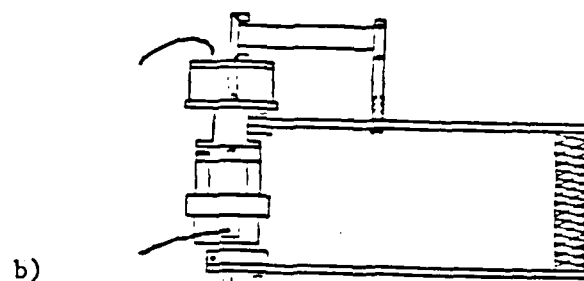
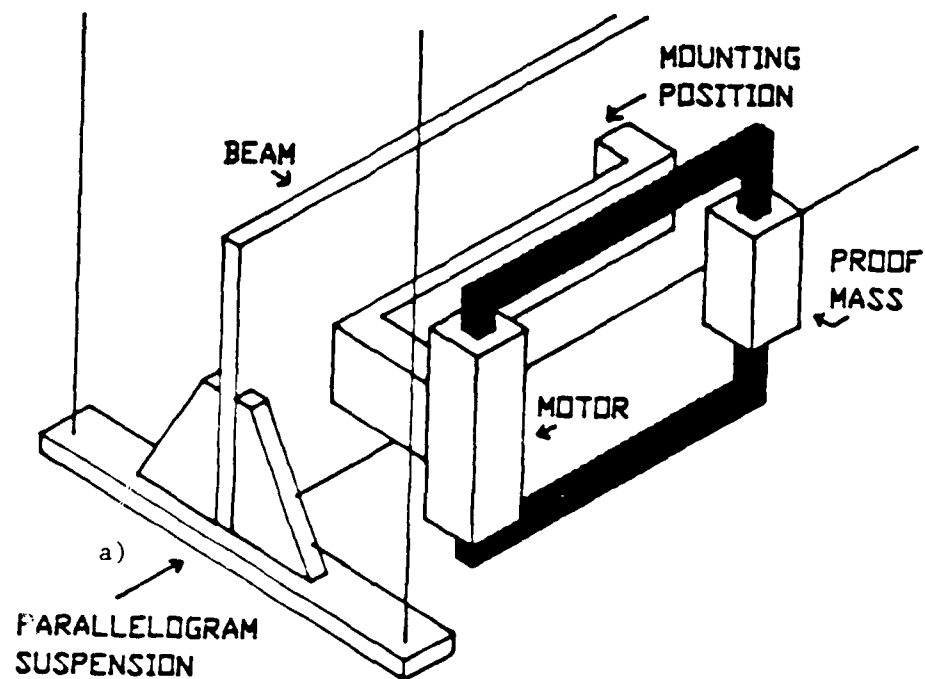


Figure 5 a) Swinging Parallelogram Beam Suspension with Actuator Placement and b) Inertial Reaction Absorber/Actuator Configuration.

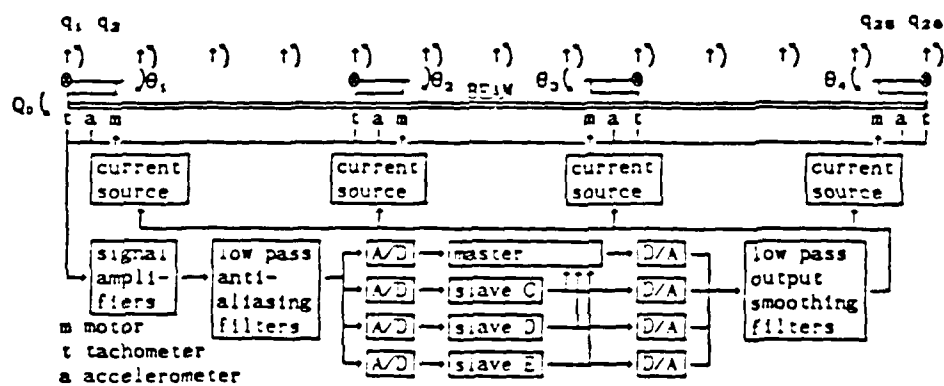


Figure 6 Control Hardware Configuration and Modeled DOFs for Experimental Phase.

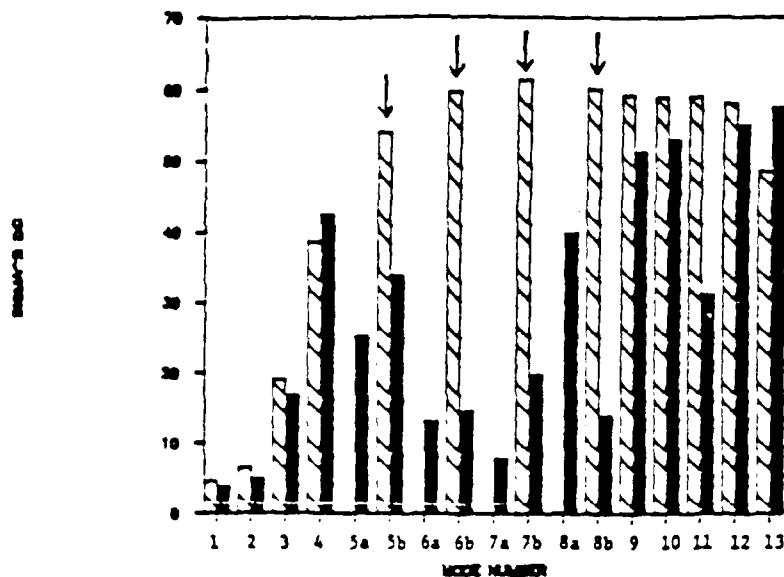


Figure 7 Level of Disturbance Transmission to the Model States for the System Without (hatched) and With (solid) Absorbers Tuned to Target Modes.

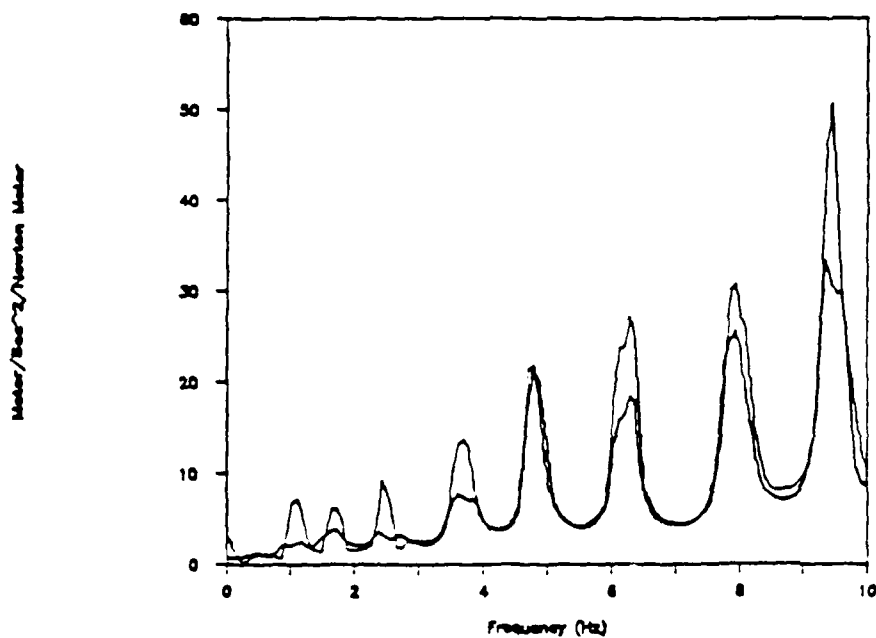


Figure 8 Acceleration Transfer Function a) with Very Stiff Absorbers (higher level response) and b) with Tuned Absorbers (lower level response).



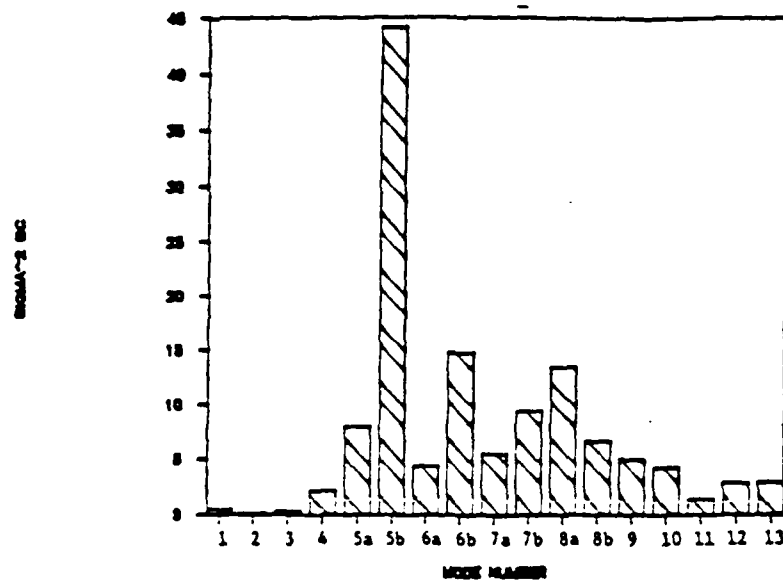


Figure 9 Level of Control Transmission to the Model States for the System with Absorbers Whose Passive Components are Tuned to Those of an Optimal Absorber.

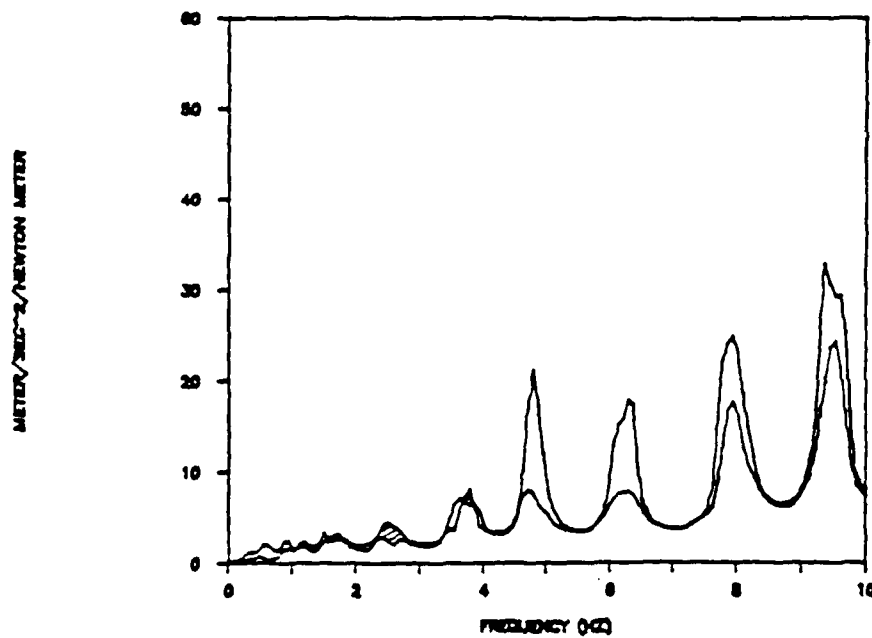


Figure 10 Acceleration Transfer Function a) with Tuned Absorbers (higher level response) and b) with Uniform Dual Feedback to Tuned Actuators. Hatching indicates regions in which response is increased in case b.

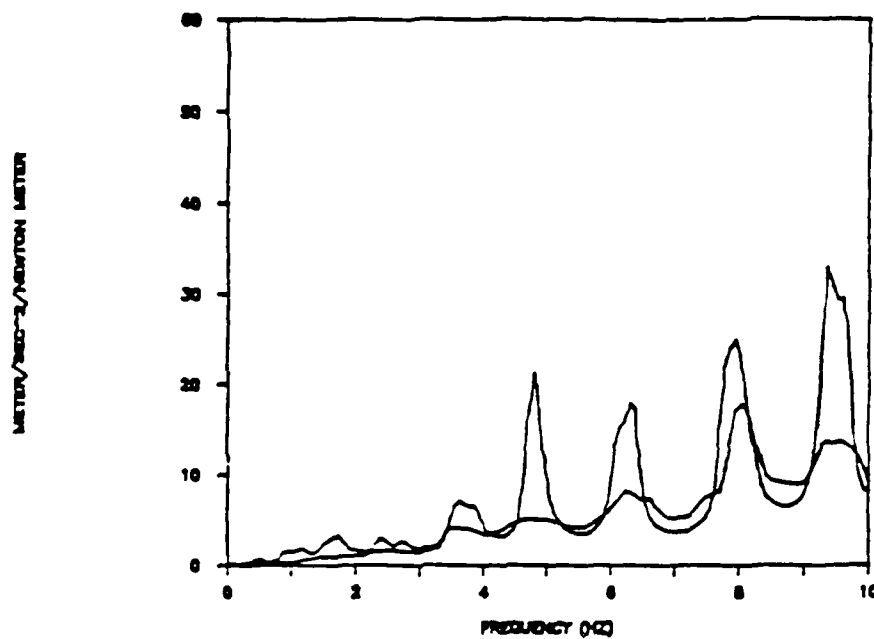


Figure 11 Acceleration Transfer Function a) with Tuned Absorbers (higher level response) and b) with Colocated Rate Feedback to a Single Actuator Reacting Against the Laboratory Frame (lower level response).

## APPENDIX 2:

### A PROCEDURE FOR CALCULATING THE DAMPING IN MULTI-ELEMENT SPACE STRUCTURES

Edward F. Crawley and Kevin J. O'Donnell

Department of Aeronautics and Astronautics  
Massachusetts Institute of Technology  
Cambridge, Massachusetts USA

#### ABSTRACT

A procedure is outlined for estimating the damping in a multi-element space structure by incorporating distributed material damping and discrete nonlinear joint properties into a linear analysis. Tests have been conducted in which the transient response of a truss member is measured in free fall in a vacuum in order to obtain precise material damping characteristics. The force-state mapping technique is then used to identify the localized nonlinearities in joints by mapping the force transmitted through the joint as a function of the full mechanical state of the joint. The identified nonlinear joint parameters are then linearized using an equivalent energy approach which finds the equivalent linear stiffness and linear viscous damping by equating the integrated work done and energy dissipated by the nonlinearity to those of a spring and damper undergoing sinusoidal motion. The distributed material damping and localized nonlinear effects are then incorporated to form a linearized damped finite element model. Finally, an eigenvalue perturbation analysis is developed to explore the effect of introducing damping at the joints on the overall dynamics of the truss, and to obtain design guidance on where supplemental joint damping might optimally be added.

#### KEYWORDS

Structural damping; material damping measurements; nonlinear identification; equivalent energy linearization; eigenvalue perturbation; multi-element structure analysis.

#### INTRODUCTION

One of the important remaining challenges in the development of structural dynamic analytic tools is the ability to predict, *a priori*, the damping of a structure. What is measured as damping in a structure is actually a combination of two phenomena, energy loss due to transmission out of the structure and true dissipation within the structure. Transmission losses occur at the structural support interface (Dowell, 1986) and by aerodynamic and acoustic transmission to the surrounding air. True dissipation occurs in a distributed sense throughout the material and due to localized nonlinearities at a discrete number of joints and fittings in mechanical contact.

For space structures in the vacuum and zero gravity of space, only true internal dissipation need be considered since transmission losses are insignificant. This is a fortunate coincidence, since it is for space structures that an accurate *a priori* prediction of damping and the nonlinear effects of joints is most important. The potential interaction of the flexible structure with the control system makes it necessary to have accurate knowledge of the damping to assure a robust controller at high gains. However, the large size and/or flexibility of envisioned space structures makes ground vibration testing difficult. Even if ground testing is performed, the need to suspend the structure, the presence of gravity loads on the joints, and the air damping make it difficult to directly extrapolate the measured damping results to the space environment. Thus the modeling and prediction of damping in space structures is an important area for analytic development. The repetitive nature of elements and joints in contemporary space structures makes feasible the development of such an analysis at this time.

The approach taken by this paper is to assume that a linear undamped analytic or numerical model of the structure already exists. A procedure is presented for incorporating first the material damping and then the joint effects to obtain a more complete damped model of the structure (Fig. 1). The material damping properties of the constituent truss material must first be measured. This material damping is the fundamental damping inherent in the final assembled structure regardless of how the elements are joined. The potentially nonlinear behavior of the joints must then be measured in such a way as to provide an adequate dynamic characterization. These nonlinear effects must then be linearized and incorporated into the

overall model. For confidence that the model can accurately predict the behavior of an assembled space structure, the completed model should be verified by ground and space based dynamic testing.

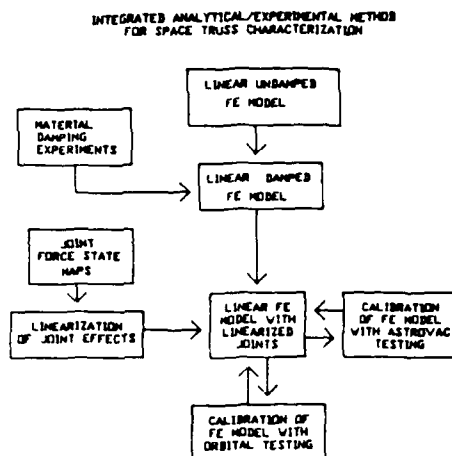


Fig. 1 Block diagram of the incorporation of material damping and localized nonlinearities into a linear undamped finite element model.

#### MATERIAL DAMPING

The material damping in a truss element is a distributed property of the material. Two possible approaches can be considered when trying to incorporate the effects of material damping into a structural model: a fundamental micromechanical approach; or a phenomenological approach.

The fundamental micromechanical approach attempts to identify the physical basis of the dissipation at a micromechanical level and predict from first principles the material dissipation. Some micromechanical models are relatively simple. For example, for isotropic anelastic metals, Zener (1948) postulated that material damping arises when the time dependent stress and strain in the material are not in phase due to transverse heat flow. As a result, the damping depends upon the relative frequency of vibration compared to the transverse relaxation frequency, the frequency associated with the time constant of transverse thermal transport. Thermal transport damping can be considered a fundamental or background damping mechanism present even at low amplitudes, but is in no way the only one present. At high strain amplitudes, dissipation in metals often increases due to losses suspected to be associated with grain boundary and inclusion motion. In graphite/epoxy composite materials, the visco-elasticity of the matrix is a key contributor to the material dissipation (Adams, 1986). In metal matrix materials, the fiber, metal matrix, and interface bonding can all contribute to the dissipation (Rawal and Misra, 1986). Lazan (1964) made a classic study of such mechanisms.

When the ultimate objective is to predict the damping in a complex structure, an approximate phenomenological approach to the quantification of material damping is preferable for a variety of reasons. First, the fundamental physical models are often complex, diverse, and inexact. Second, they must often be verified or calibrated by test, producing a data base on damping which can just as easily be approximated by a phenomenological model. Third, in the final analysis, the material damping is often small compared to the eventual structural damping due to the joints and attachments. Therefore, a more approximate model is justifiable.

The difficulty in obtaining material damping data is that the damping is generally up to an order of magnitude smaller than aerodynamic damping or damping due to energy transmission into the supporting structure of the specimen. One approach to the measurement of material damping which eliminates this experimental interference is to examine the vibration in free fall in a vacuum. To accomplish this, an apparatus called the Tunable Excitation Launch Mechanism (TELM) was developed in which a material specimen can be lofted with a specified initial strain level in a vacuum while measuring its transient response, from which the material damping ratio can be obtained (Crawley and Mohr, 1985). By changing specimens and excitation amplitudes, the material damping can be measured as a function of frequency, strain, and specimen geometry.

A variety of phenomenological models have been developed based on testing at MIT and elsewhere. Tests conducted on Aluminum 2024-T3 showed that the Zener prediction was very good for specimens with frequencies above the relaxation frequency of the aluminum (Fig. 2). However, the tests below the relaxation frequency showed an exponential dependence of damping on strain which is not predicted by the Zener model (Crawley and van Schoor, 1986). For metal matrix materials with low loss fibers and good fiber matrix bonding, such as graphite/aluminum, the

material damping in the composite can be associated with the matrix dissipation (Crawley and van Schoor, 1986). In Fig. 3, the damping in graphite/aluminum shows the same frequency dependence as predicted by the Zener model for a pure aluminum bar. Damping in graphite/epoxy materials tends to be relatively independent of strain or frequency, but strongly dependent on laminant ply orientation and stacking (Adams, 1986).

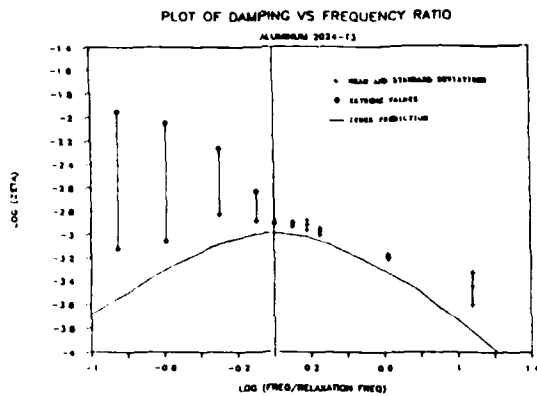


Fig. 2 Comparison of material damping measurements with the Zener prediction for aluminum 2024-T3.

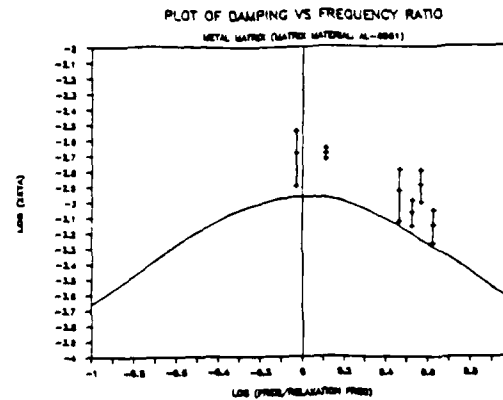


Fig. 3 Comparison of material damping measurements with the Zener prediction for metal matrix composites.

With sufficient experimentation, an appropriate phenomenological model of the damping in the structural material can be developed. The data which best represents the strain levels and frequencies appropriate to the elements of the complete structure can then be incorporated into the linear undamped finite element model to create a linear damped model. Given the distributed nature of the damping and its small value, the complex modulus ( $1+ig$ ) modal damping is considered an acceptable method of incorporating the material damping. The damping parameter  $g$  will, in general, depend on frequency and the average strain in the particular element. If these parameters are not relatively constant or small, iteration may be necessary to achieve the appropriate value of  $g$ . Once this is accomplished, the remaining tasks are to identify and incorporate into the structural model the effects of the joint nonlinearities, which are generally expected to dominate the total structural damping.

#### NONLINEAR IDENTIFICATION

Joints of deployed or assembled spacecraft generally have some form of pin, ball, or sliding or interlocking mechanism, and may or may not be preloaded in their final form. Such joints are seen as a potential source of nonlinearities, such as impacting and friction between contacting surfaces.

The force-stroke technique (Soni and Agrawal, 1985; Belvin, 1985) has been commonly used to identify nonlinear stiffness effects in joints. The technique identifies the behavior by plotting the quasi-steady force applied to the joint versus the resulting displacement. As the name implies, no rate dependent effects are included in this type of identification. Without explicit rate dependent information, the force-stroke data cannot discern between systems with state dependent energy dissipation, such as linear viscous damping, and systems with true memory dependent dissipation, such as viscoelasticity, (O'Donnell and Crawley, 1985).

As an alternative to force-stroke testing, an extension of the technique known as force-state mapping has been developed (Crawley and O'Donnell, 1986). In this technique, the force transmitted by the joint is represented as a function of the relative displacement and velocity across the joint; i.e., as a function of the full mechanical state of the joint. As an example of this technique, consider a joint modeled as a single degree of freedom spring mass damper system, where the spring and damper are properties of the joint, and the mass represents the mass of the adjacent truss element. The dynamics of this model can be represented by the memoryless ordinary nonlinear second order equation of motion

$$M \ddot{x} + B(x, \dot{x}) \dot{x} + K(x, \dot{x}) x = F(t) \quad (1)$$

where the generalized damping and stiffness  $B$  and  $K$  can vary as a function of the state. Regrouping the terms of Eqn. (1) gives

$$F_r(x, \dot{x}) = F(t) - M \ddot{x} = B(x, \dot{x}) \dot{x} + K(x, \dot{x}) x \quad (2)$$

where  $F_r$  represents the force transmitted by the joint entirely as a function of the instantaneous state of the joint.

To produce a force-state map, the transmitted force is calculated at each measurement interval as the measured applied force minus the mass times the measured acceleration. The transmitted

force is then plotted versus the measured displacement and velocity. The force-state map of a general linear spring mass damper system would be a plane whose slope with respect to displacement would be the linear stiffness  $K$  and with respect to velocity would be the linear viscous damping  $B$  (Fig. 4). Any deviation in a force-state map from a flat plane is an indication of a nonlinearity in the system.

An interesting property of the force-state mapping formulation is that any nonlinearities in the system represented by the right hand side of Eqn. (2) are superposable. Therefore, the transmitted force can be expressed as a linear combination of linear and nonlinear force components. A representative but not exhaustive list of common force components is given as

$$F_t = C + K_1 x + B_1 \dot{x} + K_n x^n + B_n \dot{x}^n + K_{0s} + B_{0s} + F_s \text{sign}(\dot{x}) + g|x|\text{sign}(\dot{x}) \quad (3)$$

where

$$K_{0s} = \begin{cases} k_{0s}(x-x_{0s}) & x_{0s} \leq x \\ 0 & -x_{0s} \leq x \leq x_{0s} \\ k_{0s}(x+x_{0s}) & x \leq -x_{0s} \end{cases}, \quad B_{0s} = \begin{cases} b_{0s}(\dot{x}) & x_{0s} \leq x \\ 0 & -x_{0s} \leq x \leq x_{0s} \\ b_{0s}(\dot{x}) & x \leq -x_{0s} \end{cases}$$

The first three terms of Eqn. (3) represent a constant preload, a linear spring, and a linear damper. The next two terms represent higher order springs and dampers, the sixth and seventh terms deadband springs and dampers, the eighth classical Coulomb friction, and the last classical (1+ig) material "hysteresis" damping and displacement dependent friction (Hertz and Crawley, 1985). It should be emphasized that while Eqn. (3) contains most of the effects which contribute to so called "hysteresis" or "memory" effects on a conventional force-stroke plot, they are in fact not true memory effects, but depend only on the instantaneous state. Therefore, each will produce a distinct, unique, and superposable surface on a force-state map, independent of the amplitude, frequency, or time history of the test.

A two-part procedure for identifying the force-state characteristics of joints can now be outlined. The first step is to produce a force-state map of a joint or other structure using Eqn. (2) with data derived from a suitable experiment. The second step is the actual identification of system parameters by decomposing the force-state map into the force components listed in Eqn. (3) by a least squares fitting procedure. The latter part of this process is demonstrated on the force-state map of an actual pinned clevis joint with a restraining sleeve (Fig. 5).

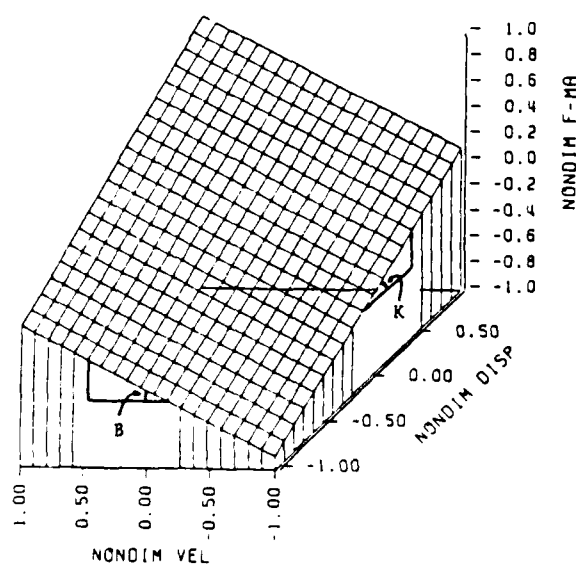


Fig. 4 Force-state map of an ideal linear spring mass damper system.

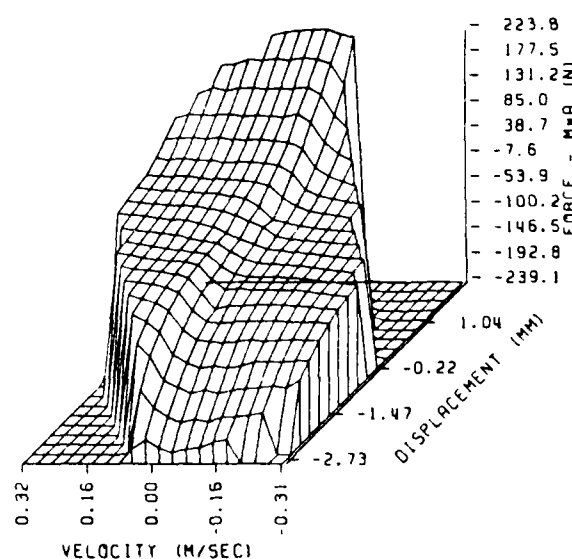


Fig. 5 Force-state map of a pinned clevis joint with a restraining sleeve.

The original two dimensional projection of the force-state map onto the force-displacement plane and the recreated versions are shown in Fig. 6. The first fit is a simple linear and cubic spring function which closely matches the shape but has no dissipative properties. The second fit then includes friction and produces the expected hysteresis step when the displacement changes direction; i.e., when the velocity changes sign. Finally, with the addition of linear viscous damping, the fourth graph becomes the fully reconstructed signal. Note that the transmitted force characteristics have been very accurately reproduced, and what might have originally appeared as a memory effect has been well represented with state dependent linear viscous damping plus Coulomb friction.

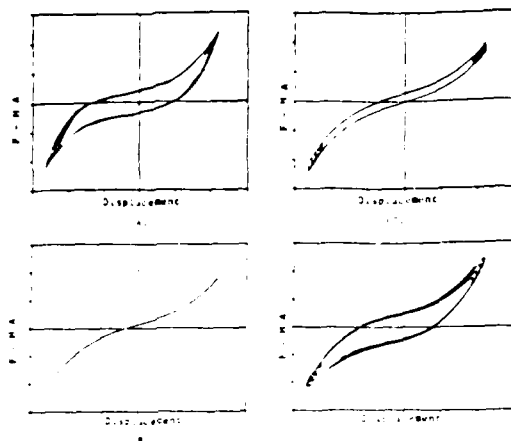


Fig. 6 Reconstruction of the two-dimensional projection of Figure 5 using the identified fit parameters.

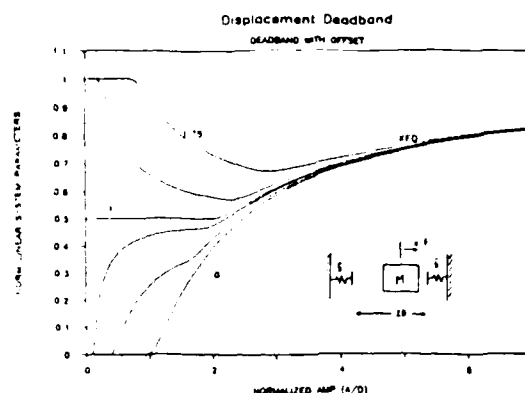


Fig. 7 Equivalent energy linearization of a deadband spring parameterized by the normalized initial offset from the center of the deadband.

The force-state mapping technique has been shown to provide a method for characterizing the behavior of joints as a function of the full mechanical state of the joint. Using this technique, particular types of nonlinearities can be recognized and physical insight gained by examining the force-state map. The nonlinearities can be identified by appropriately decomposing the force-state map into a linear combination of linear and nonlinear force components.

#### INCORPORATION OF NONLINEAR EFFECTS

##### Equivalent Energy Linearization

Once the linear and nonlinear properties of the joints have been identified, the linear damped finite element model can be updated with the identified linear stiffness and damping terms associated with the joints. This will produce a modified linear damped finite element model; however, the nonlinear terms must still somehow be included. Four techniques have been examined for use in linearizing the nonlinear terms: a direct least squares fit of a plane to a localized region of the force-state map; the method of harmonic balance; a temporal Galerkin technique (Timoshenko, Young, and Weaver, 1974; Griffin, 1980); and a method based on equivalent energy (Meirovich, 1975). Of these techniques, the direct least squares approach has been shown to produce incorrect linearizations for use in dynamic modeling (O'Donnell and Crawley, 1986). The remaining three techniques are similar and yield the same correct linearization in the case of steady state sinusoidal motion.

Of these three, the equivalent energy linearization technique provides both a direct functional form for the linearized coefficient and physical insight into the nature of the nonlinearity. The technique is based on finding the amplitude and frequency dependent equivalent stiffness and damping terms ( $K_{eq}$  and  $C_{eq}$ ) which have equivalent work and energy dissipation over a complete cycle as the nonlinear force. The integral representation of this is given by

$$\int_0^T (K_{eq} \dot{x}) \dot{x} dt = \int_0^T F(x, \dot{x}) \dot{x} dt \quad (4) \quad \int_0^T (C_{eq} \dot{x}) \dot{x} dt = \int_0^T F(x, \dot{x}) \dot{x} dt \quad (5)$$

The integrals are then solved for the unknown parameters  $K_{eq}$  and  $C_{eq}$  for each type of nonlinearity  $F(x, \dot{x})$ . For assumed steady state sinusoidal motion,  $x(t) = A \cos(\Omega t)$ , Eqns. (4) and (5) reduce to

$$K_{eq} = \frac{\Omega}{\pi A^2} \int_0^T F(x, \dot{x}) \dot{x} dt \quad (6) \quad C_{eq} = \frac{1/\Omega}{\pi A^2} \int_0^T F(x, \dot{x}) \dot{x} dt \quad (7)$$

In this way, the linearized coefficients are reduced to simple functions of the amplitude and frequency.

As an example of the usefulness of this technique, consider the equivalent energy linearization of a deadband spring (Fig. 7). In this case, the equivalent stiffness is frequency independent and is plotted versus the amplitude of motion normalized by half the deadband gap. The curves are also parameterized by an initial displacement offset (possibly due to a gravity preload) also normalized by half the deadband gap. The equivalent spring has no effect on the system until the value of the initial offset plus the amplitude exceeds one; i.e., the spring does not influence the mass until the mass contacts it. When the initial offset is greater than the deadband gap, the equivalent stiffness will decrease for a range of amplitudes when the mass enters the deadband, but will eventually again increase toward the limit of the deadband spring constant. One of the benefits of the equivalent energy technique is the creation of these equivalent parameter plots which provide useful physical insight into the nature of the nonlinearity.

To verify the accuracy of the equivalent linearization approach, a comparison is made between the exact solution for the response of a spring mass Coulomb friction damper with the response calculated using the equivalent linear damper. The exact solution exists only for certain ranges of nondimensional friction values (Den Hartog, 1931). The comparison is shown in Fig. 8 parameterized by  $F/Q$ , the friction value normalized by the applied force amplitude. The system also has 5 % linear viscous damping. The dashed line indicates the amplitudes above which the analytic solution is valid. The comparison in Fig. 8 indicates excellent agreement of the linearized solution and exact solution even for relatively large values of friction.

Once the nonlinearities have been appropriately linearized, they must then be included into the updated finite element model. Since the linearized stiffness and damping may be amplitude and/or frequency dependent, the exact value of the linearized coefficients must be determined iteratively. To accomplish this, the frequency response of the linear system without the nonlinear parameters is first determined for a fixed excitation level. The amplitude and frequency are then used to update the damping and stiffness matrices with the linearized parameters to create a new linear damped model. The procedure is repeated until the desired convergence has been achieved. For large nonlinear effects, this technique may need to be modified to guarantee convergence.

### Eigenvalue Perturbation Solution

Since the equivalent linearized parameters derived above are expected to exert a relatively small influence on the dynamics of the structure, it is natural to consider the effects of material damping and nonlinearities as small perturbations about the undamped linear system. In this situation, an eigenvalue perturbation technique can be used to determine the general behavior of the system subjected to small changes (Hagedorn, 1983). This treatment of the damping as a perturbation problem would greatly reduce the computational burden of recomputing the full order eigenvalue problem at each cycle of iteration. The perturbation analysis can also be used in estimating the effects of damping and as a design tool for guidance in determining the best locations to design deliberate joint damping into a structure.

As an example of the application of the perturbation technique, consider the undamped matrix representation of a structure

$$\mathbf{M} \ddot{\mathbf{q}} + \mathbf{K} \mathbf{q} = 0 \quad (9)$$

Now when the effects of damping are included, but are small compared to the inertial and stiffness terms, the equation of motion becomes

$$\mathbf{M} \ddot{\mathbf{q}} + \zeta \mathbf{B} \dot{\mathbf{q}} + \mathbf{K} \mathbf{q} = 0 \quad (9)$$

where  $\zeta$  is a small parameter such that the damping effect is small compared to either of the other two terms in the equation. Additionally, it is required that  $\mathbf{M}$  is positive definite and symmetric and that  $\mathbf{K}$  is positive semi-definite and symmetric. The requirement that  $\mathbf{M}$  and  $\mathbf{K}$  be symmetric is purely to simplify the analysis, which can be extended to nonsymmetric system matrices with the use of right and left eigenvectors. To solve for the perturbed eigenvalue solution, express the  $k^{\text{th}}$  eigenvalue,  $\lambda^{(k)}$ , and eigenvector,  $\psi^{(k)}$ , as an expansion in terms of the small parameter  $\zeta$

$$\lambda^{(k)} = \lambda_0^{(k)} + \zeta \lambda_1^{(k)} + \zeta^2 \lambda_2^{(k)} + \dots \quad (10)$$

$$\psi^{(k)} = \psi_0^{(k)} + \zeta \psi_1^{(k)} + \zeta^2 \psi_2^{(k)} + \dots \quad (11)$$

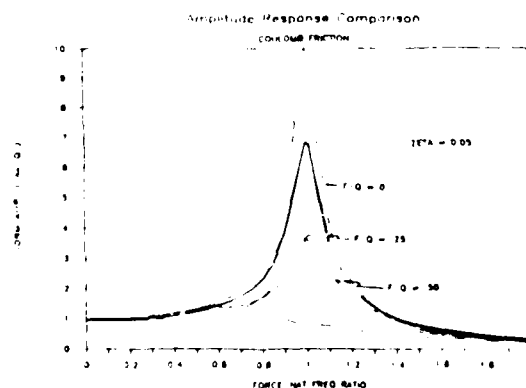


Fig. 8 Response amplitude of a spring mass system with friction using the linearized damping compared to the analytic solution;  $\zeta = 0.05$ .

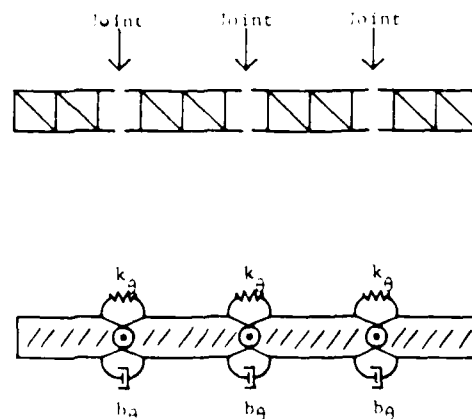


Fig. 9 Simple truss whose joints are modeled as linear springs and dampers.



When  $q = \varphi \exp(\lambda t)$ , the solution to Eqn. (9) is a quadratic eigenvalue problem with increasing powers of  $\zeta$ . Since  $\zeta$  is assumed to be small, the resulting problem can be solved successively by equating those terms which multiply like powers of  $\zeta$ . The first two equations, corresponding to  $\zeta^0$  and  $\zeta^1$  become

$$(\lambda_0^2 \mathbf{M} + \mathbf{K}) \cdot \varphi_0 = 0 \quad (12)$$

$$(\lambda_0^2 \mathbf{M} + \mathbf{K}) \cdot \varphi_1 + \lambda_0 (2\lambda_1 \mathbf{M} + \mathbf{B}) \cdot \varphi_0 = 0 \quad (13)$$

where the superscripts have been dropped for brevity. Equation (12) is the zeroth order eigenvalue problem which is assumed to have already been solved. The second and all subsequent equations are simply linear equations and do not involve solving additional eigenvalue problems. While Eqn. (13) and all that follow from the perturbation analysis each introduce a new  $\lambda$  and  $\varphi$  as unknowns, appropriately normalized orthogonality conditions can be used to eliminate the new eigenvectors in terms of the zeroth order eigenvectors. Each equation can then be used to produce another eigenvalue perturbation.

Given that  $\mathbf{M}$  and  $\mathbf{K}$  are both symmetric, the zeroth order eigenvectors can be normalized so that the orthogonality conditions hold

$$\varphi_{0i}^T \cdot \mathbf{M} \cdot \varphi_{0j} = \delta_{ij} \quad (14)$$

$$\varphi_{0i}^T \cdot \mathbf{K} \cdot \varphi_{0j} = \delta_{ij} \omega_i^2 \quad (15)$$

where  $\omega_i = -i \lambda_0^{(k)}$  are the undamped frequencies from Eqn. (12). The first eigenvalue perturbation is given by

$$\lambda_1^{(k)} = -1/2 \omega_k b_{kk} \quad (16)$$

with

$$b_{ek} = \varphi_{0e}^T \cdot \mathbf{B} \cdot \varphi_{0k} \quad ; \quad e, k = 1, 2, \dots, N \quad (17)$$

where  $N$  is the dimension of the matrices in Eqn. (14). Therefore, to first order in  $\zeta$ , the complete eigenvalue can be rewritten as

$$\lambda^{(k)} \approx \omega_k \left[ 1 - 1/2 \zeta b_{kk} \right] \quad (18)$$

Note that the first perturbation is purely real and negative for  $\mathbf{B}$  positive definite. This shows that a small increase in damping causes a proportionally small shift of the poles to the left in the complex plane; i.e., proportionally increasing the damping in the modes.

If additional damping is to be added at the joints, Eqns. (16) through (18) provide useful design guidance in choosing the location and strength of joint dampers. If the  $k^{\text{th}}$  mode is to be the target for damping, Eqn. (17) implies that the location and strength of the dampers; i.e., the  $\mathbf{B}$  matrix entries, must be chosen so that the product  $\varphi_{0i}^T \cdot \mathbf{B} \cdot \varphi_{0i}$  is maximized. Physically this means that the damping must be placed at locations of high relative motion of the mode.

For the case of nonrepeated eigenvalues, the first and all subsequent perturbations are obtained from simple multiplications and additions of known matrices and do not require additional eigenvalue solutions or matrix inversions. For this situation, the second eigenvalue perturbation becomes

$$\lambda_2^{(k)} = -\frac{i\omega_k}{2} \left\{ \sum_{e \neq k} \frac{b_{ke} b_{ek}}{\omega_k^2 - \omega_e^2} + \left[ \frac{b_{kk}}{2\omega_k} \right]^2 \right\} \quad (19)$$

For the case of repeated nonzero eigenvalues, additional eigenvalue problems of the order of the degeneracy need to be solved (Hagedorn, 1983). For repeated zero eigenvalues (rigid body modes), the matrix problem can be reduced by diagonalizing Eqn. (8); i.e., transforming to modal coordinates, and removing the rigid body equations. This is equivalent to perturbing the eigenvalues only on the reduced subspace of the flexible modes and is valid since structural damping will not affect the rigid body frequencies or mode shapes.

Using the procedure described above, the perturbed eigenvalues of a thirteen degree of freedom, four element beam (Fig. 9) were calculated and compared to the exact solution obtained using the EISPACK eigenvalue problem subroutines. Each element of the beam had a compatible end translation with its neighbor, simulating pinned joints between elements. The elements were connected rotationally at the joints with rotational springs and dampers. The problem was nondimensionalized using the characteristic length, time, and stiffness of a single beam element. The joint stiffness ( $k_\theta$ ) was chosen to be 0.3, 1.0, and 3.0 times the element stiffness  $EI/L$ , intended to span a realistic range of joint stiffness. The design parameter which was varied was the amount of rotational joint damping ( $b_\theta$ ). With finite joint stiffness, this model has eleven flexible modes and two rigid body modes. Since the rigid body modes correspond to repeated zero eigenvalues, the original  $13 \times 13$  problem was diagonalized using the undamped mode shapes and the two rigid body equations were removed.

The exact locations of the eleven flexible mode poles were computed with the EISPACK subroutines for joint stiffness ratios ( $k_j/EI/l$ ) of 0.3, 1.0, and 3.0 with varying joint damping. The results with the stiffness ratio of 1.0 are shown in Fig. 10. Three distinct types of behavior of the poles can be observed as the joint damping is increased from zero. The first (I) is when poles move approximately along a quarter circle from the imaginary axis toward the real axis (modes 10 and 11 in Fig. 10). This behavior is indicative of modes in which joint motion dominates the mode shape, and is similar to the behavior when proportional damping is added to a mode. The second type of behavior (II) is when poles move along a "semicircle" first away from and then back toward the imaginary axis with either increasing or decreasing frequency as in modes 8 and 9 in Fig. 10. The final most complex type of behavior (III) is when a pole initially curves up or down but then "changes direction" and returns to the real axis or imaginary axis (mode 7 in Fig. 10).

The predicted locations of the flexible mode poles was also obtained using the first and second perturbations of the eigenvalue as given in Eqns. (16) and (19). A comparison of the predicted and exact pole locations of the seventh flexible mode for the three joint stiffness ratios is shown in Fig. 11. This mode displays all three types of behavior described above as the damping in the joints is increased, depending on the relative stiffness of the joint compared to the beam element. For low joint stiffness (the lowest path in Fig. 11), the mode is dominated by joint motion and damps quickly (I). For high joint stiffness (the highest path), the mode behaves like (II) with increased damping. For a moderate joint stiffness, the pole is in transition (III) between the other two types of behavior. However, even though the quadratic form of the estimate cannot accurately model the behavior of (II) and (III) for large damping, perturbation analysis is almost exact for realistic levels of joint stiffness, and structural damping levels up to 5 %.

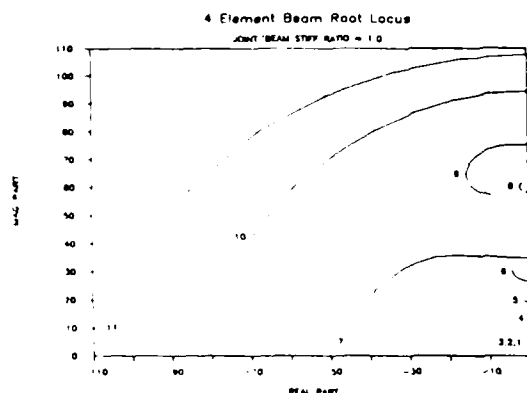


Fig. 10 Root locus of a four element truss as the linear joint damping is increased from zero; joint stiffness ratio = 1.0.

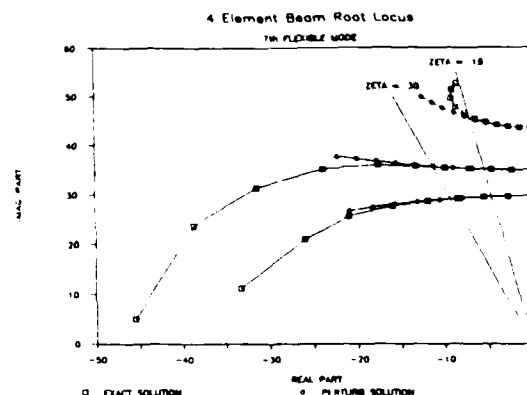


Fig. 11 Comparison of the exact and perturbation pole location of the seventh flexible mode of a four element truss.

#### SUMMARY

When analyzing the effects of multi-element space structures connected by joints, four distinct steps are required to fully account for material and nonlinear effects. The first step involves creation of a linear undamped finite element model. In the second step, the material damping properties of each element are determined and incorporated through a complex modulus representation to create the linear damped finite element model of the structure. The third step is the identification of the nonlinear joint properties using the force-state mapping technique. The identified nonlinear components are then linearized using the equivalent energy method in the fourth step. The linearization is incorporated into the linear damped model through iteration to create the linearized damped finite element model. The perturbation analysis has shown that changes in the modal damping can be accurately calculated using only the first eigenvalue perturbation (Eqn. 16). Additionally, the perturbation analysis provides an excellent design tool by providing quick estimates of the structural damping and by providing guidance in choosing the value and location of additional dampers to provide optimal modal damping in specific target modes.

#### ACKNOWLEDGEMENTS

This research was supported by NASA Grant # NAGW-21 from NASA Headquarters, Washington, D.C., with Mr. Samuel Vennert serving as technical monitor and by the McDonnell Douglas Astronautics Corporation with Mr. James Peebles as technical monitor.

## REFERENCES

- Adams, R.D. (1986). A Review of the Damping Mechanisms in Advanced Fibre-Reinforced Composites. *Proceedings of the Vibration Damping Workshop II*, Las Vegas, NV.
- Belvin, W.K. (1985). Modeling of Joints for the Dynamic Analysis of Truss Structures. Master of Science Thesis, School of Engineering and Applied Science, VPI&SU, Blacksburg, VA.
- Crawley, E.F. and D.G. Mohr (1985). Experimental Measurements of Material Damping in Free Fall with Tunable Excitation. *AIAA Journal*, **23** (1), 125-131.
- Crawley, E.F. and K.J. O'Donnell (1986). Identification of Nonlinear System Parameters in Joints Using the Force-State Mapping Technique. *AIAA Paper 86-1013-CP*, 27th Structures, Structural Dynamics and Materials Conference, San Antonio, TX.
- Crawley, E.F. and M.C. van Schoor (1986). Material Damping in Aluminum and Metal Matrix Composites. *Proceedings of the Vibration Damping Workshop II*, Las Vegas, NV.
- Den Hartog, J.P. (1931). Forced Vibrations with Combined Coulomb and Viscous Friction. *Transactions of the ASME*, **53**, APM-107.
- Dowell, E.H. (1986). Damping in Beams and Plates due to Slipping at the Support Boundaries. *Journal of Sound and Vibration*, **105** (2), 243-253.
- Griffin, J.H. (1980). Friction Damping of Resonant Stresses in Gas Turbine Engine Airfoils. *Journal of Engineering for Power*, **102**, 329-33.
- Hagedorn, P. (1983). The Eigenvalue Problem for a Certain Discrete Class of Linear Systems: A Perturbation Approach. *Proceedings from the Fourth Symposium of Dynamics and Control of Large Structures*, VPI&SU, Blacksburg, VA, p. 355.
- Hertz, T.J. and E.F. Crawley (1985). Displacement Dependent Friction in Space Structure Joints. *AIAA Journal*, **24** (12), 1998-2000.
- Lazan, B.J. (1964). Damping Mechanisms and Phenomenology in Materials. *Proceedings of the Eleventh International Congress of Applied Mechanics*, Munich.
- Meirovich, L. (1975). *Elements of Vibration Analysis*. McGraw-Hill, Inc.
- O'Donnell, K.J. and E.F. Crawley (1985). Identification of Nonlinear System Parameters in Space Structure Joint Elements Using the Force-State Mapping Technique. MIT SSL Report #16-85.
- O'Donnell, K.J. and E.F. Crawley (1986). The Use of Equivalent Linearization and Eigenvalue Perturbation Methods in Space Structure Design. MIT SSL Report #9-86.
- Rawal, S. and M.S. Misra (1986). Material Damping in Space Structures. *Proceedings of the Vibration Damping Workshop II*, Las Vegas, NV.
- Soni, M.L. and B.N. Agrawal (1985). Damping Synthesis for Flexible Space Structures Using Combined Experimental and Analytical Models. *AIAA Paper 85-0779*, 26th Structures, Structural Dynamics and Materials Conference, Orlando, FL.
- Timoshenko, S., D.H. Young, and W. Weaver (1974). *Vibration Problems in Engineering*. John Wiley and Sons, Inc.
- Zener, C.M. (1948). *Elasticity and Anelasticity of Metals*. University of Chicago Press, Chicago, IL.

END

5-87

DTIC